Atmos. Chem. Phys. Discuss., 10, 25991–26044, 2010
www.atmos-chem-phys-discuss.net/10/25991/2010/
doi:10.5194/acpd-10-25991-2010

Atmospheric Chemistry and Physics Discussions

Hygroscopic properties of atmospheric aerosol particles over the Eastern Mediterranean: implications for regional direct radiative forcing under clean and polluted conditions

M. Stock[1], Y. F. Cheng[1,*], W. Birmili[1], A. Massling[1,], B. Wehner[1], T. Müller[1], S. Leinert[2], N. Kalivitis[3], N. Mihalopoulos[3], and A. Wiedensohler[1]**

[1]Leibniz Institute for Tropospheric Research, Leipzig, Germany
[2]Environmental Protection Agency, Dublin 14, Ireland
[3]Environmental Chemical Processes Laboratory, University of Crete, Heraklion, Greece
[*]now at: Center of Global and Regional Environment Research, Univ. of Iowa, Iowa City, USA
[**]now at: National Environmental Research Institute, Aarhus University, Roskilde, Denmark

Received: 14 October 2010 – Accepted: 25 October 2010 – Published: 3 November 2010

Correspondence to: W. Birmili (birmili@tropos.de)

Published by Copernicus Publications on behalf of the European Geosciences Union.

Abstract

This work examines the effect of direct radiative forcing of aerosols in the eastern Mediterranean troposphere as a function of air mass composition, particle size distribution and hygroscopicity, and relative humidity (RH). During intensive field measurements on the island of Crete, Greece, the hygroscopic properties of atmospheric particles were determined using a Hygroscopicity Tandem Differential Mobility Analyzer (H-TDMA) and a Hygroscopicity Differential Mobility Analyzer – Aerodynamic Particle Sizer (H-DMA-APS). Like in several studies before, the H-TDMA identified three hygroscopic sub-fractions of particles in the sub-µm range: a more hygroscopic group, a less hygroscopic group and a nearly hydrophobic particle group. The hygroscopic particle growth factors at 90% RH were a significant function of particle mobility diameter (D_p): 1.42 (± 0.05) at 30 nm compared to 1.63 (± 0.07) at 250 nm. The H-DMA-APS identified up to three hygroscopic sub-fractions at mobility diameters of 1.0 and 1.2 µm. All data recorded between 12 August and 20 October, 2005 were classified into four distinct synoptic-scale air mass types distinguishing between different regions of origin (western Mediterranean vs. the Aegean Sea) as well as the degree of continental pollution (marine vs. continentally influenced). The hygroscopic properties of particles with diameter $D_p \geq 150$ nm showed the most pronounced dependency on air mass origin, with growth factors in marine air masses exceeding those in more continentally influenced air masses. Particle size distributions and hygroscopic growth factors were employed to calculate aerosol light scattering coefficients at ambient RH using a Mie model. A main result was the pronounced enhancement of particle scattering over the eastern Mediterranean due to hygroscopic growth, both in the marine and continentally influenced air masses. When RH reached its daytime values around 70–80% in summer, up to 50–70% of the calculated visibility reduction was due to the hygroscopic growth of the particles by water compared to the effect of the dry particles alone. The estimated aerosol direct radiative forcings for both, marine and continentally influenced air masses were negative indicating a net cooling of the atmosphere due to the aerosol.

ACPD

10, 25991–26044, 2010

The radiative forcing ΔF_r was, nevertheless, dominated by the total aerosol concentration most of the time: ΔF_r was typically more negative for continentally influenced aerosols (ca. $-4\,W\,m^{-2}$) compared to rather clean marine aerosols (ca. $-1.5\,W\,m^{-2}$). When RH occasionally reached 90% in marine air, ΔF_r even reached values down to $-7\,W\,m^{-2}$. Our results emphasize, on the basis of explicit particle hygroscopicity measurements, the relevance of ambient relative humidity for the radiative forcing of regional atmospheres.

1 Introduction

In the accretive discussion on global climate change, atmospheric particles (aerosols) have been identified as a key uncertainty with respect to the global radiative balance (IPCC, 2007). Particles influence climate directly by scattering and absorbing solar radiation (Haywood and Boucher, 2000) and indirectly through their ability to act as cloud condensation nuclei (CCN), (Twomey, 1977; Ogren and Charlson, 1992). A sufficient knowledge of the microphysical properties of aerosol particles as well as the spatial distribution is a key to evaluate their effect on global climate. Experimental data, in particular, are necessary as input and validation parameters for global climate models, which assess the role of aerosols in future scenarios of global warming or cooling (Grant et al., 1999).

The hygroscopic growth behaviour of aerosol particles is one of the important parameters controlling the direct and indirect climate effects. Atmospheric particles can absorb water at relative humidities well below 100% depending on their chemical composition. Due to water uptake aerosol particles change their size and their optical properties (Tang, 1996). While the hygroscopic growth of pure soluble ionic species is known relatively accurately (Tang and Munkelwitz, 1994; Brechtel and Kreidenweis, 2000), the growth of atmospheric organic matter (Gysel et al., 2004) or complex mixtures of various substances that are typical for the atmosphere is more uncertain.

ACPD
10, 25991–26044, 2010

A quantitative discussion of the consequences of particle hygroscopicity in the eastern Mediterranean region has been scarce (Van Dingenen et al., 2005; Sciare et al., 2003; Bougiatioti et al., 2009). Especially information about hygroscopic behavior of the Mediterranean aerosol has not been available at all until very recently (Pikridas et al., 2010). A particular relevance of the eastern Mediterranean troposphere derives from the high amounts of humidity present in the atmosphere (leading to enhanced hygroscopic particle growth), and the region being located on the crossroads of European anthropogenic pollution as well as African dust emission that immerse with the regional marine aerosol (Lelieveld et al., 2002; Pikridas et al., 2010).

This paper reports novel field observations of the hygroscopic properties of fine and coarse aerosol particles representative of the East Mediterranean region. Different instrumental techniques including a H-TDMA instrument and a H-DMA-APS instrument were deployed at the Finokalia research station on Crete (Greece) to characterize the hygroscopic properties of the eastern Mediterranean aerosol fine and coarse particle size range. We further combine these data with simultaneous in-situ aerosol optical observations as well as particle number size distributions presented in an earlier paper (Kalivitis et al., 2008) to examine the role of air mass character, either marine or continentally influenced. As an application, the measured size-segregated particle hygroscopic growth factors were used in an optical radiation transfer model to investigate the influence of the prevailing ambient RH on the ambient particle scattering coefficients and therewith on the resulting aerosol direct radiative forcing.

2 Experimental

2.1 Field experiment

The field experiment ARIADNE (Aerosol Physical and Chemical Identification on Crete) was conducted during ten weeks between 12 August and 20 October, 2005 at the research station Finokalia (35.3° N, 25.7° E) on Crete, Greece. Figure 1 shows that the

ACPD
10, 25991–26044, 2010

site's location on the northern coast of Crete ensures that air is advected from the sea most of the time, thus limiting disturbances by land-based sources. The nearest urban centre is Heraklion with 150 000 inhabitants located 70 km west of Finokalia. The station is located at the top of a hilly elevation (250 m above sea level) facing the sea within the northerly wind sector between 270° to 90°. The nearest village with 10 inhabitants is at a distance of 3 km to the south of the station. No human activities can be found at a distance shorter than 15 km within the above mentioned sector. A comprehensive description of the Finokalia station and the suite of atmospheric measurements conducted there are given in Mihalopoulos et al. (1997) and on the station's website (http://finokalia.chemistry.uoc.gr).

In-situ aerosol measurements were carried out from inside a container laboratory, located at a distance of 200 m from the main building of the University of Crete's research station. Ambient air was sampled at a total flow rate of 16.7 l min^{-1} through a PM_{10} inlet placed 6 m above the ground. When entering the container, the sample aerosol was conditioned to a low-humidity state. Both Nafion^{TM} membrane diffusion dryers (model MD-110-12-F, ANSYCO Inc., Karlsruhe, Germany) and custom-made silica gel diffusion dryers were deployed to limit the relative humidity (RH) in the sampling liness below 30%. The desiccation served two purposes: first, condensation of moisture was avoided when the sample aerosol enters the air-conditioned laboratory container. Second, aerosol samples were prepared within a defined range of RH, which facilitates intercomparisons with other measurements (e.g., Bergin et al., 1997; Carrico et al., 2003).

2.2 Particle number size distributions (DMPS-APS)

A flow-controlled closed-loop Differential Mobility Particle Sizer (DMPS; Birmili et al., 1999) was used to measure particle number size distributions in the mobility diameter (D_p) range 18–800 nm. The sheath air in the DMPS was circulated in a closed loop, and maintained at an RH between 10 and 30% using a silica gel dryer. The time resolution of the DMPS was 10 min. An Aerodynamic Particle Sizer (APS; TSI Inc., St. Paul,

ACPD
10, 25991–26044, 2010

USA, Model 3321) was operated measuring the number size distributions of particles with aerodynamic diameters D_{ae} between 0.8 and 10 µm. The aerodynamic diameters D_{ae} were converted to mobility diameters D_p using an effective dry particle density of 1.7 g cm^{-3}. This particluar value is close to the bulk densities of ammonium sulphate and nitrate, the main constituents of accumulation mode particles (cf. Fig. 3 below), and reconciled the DMPS and APS distributions in their overlap region very well. We are aware that this density assumption is likely to be less accurate for the coarse mode ($D_p > 1$ µm), where sodium chloride is the main constituent.

The DMPS and APS were corrected for diffusional and gravitational losses occurring in the sampling tubes using the analytical formulae for laminar pipe flows (Willeke and Baron, 1993). DMPS and APS distributions were subsequently combined into a continuous size distribution across the full diameter range. The absolute measurement uncertainties with respect to particle counting and sizing in the DMPS are estimated to be 10% and 5%, respectively, based on laboratory calibrations. For the APS, these values were 10% and 9%, respectively (Wex, 2002).

2.3 Fine particle hygroscopicity (H-TDMA)

The hygroscopic properties of fine particles were analyzed using a Hygroscopic Tandem DMA (H-TDMA; Massling et al., 2005). Briefly, the H-TDMA consists of two sequential Differential Mobility Analyzers (DMA, Hauke medium) coupled with two Condensation Particle Counters (CPC, TSI 3010) as counting devices. The first DMA selected a monodosperse particle size fraction from the polydisperse ambient aerosol at dry conditions. Half of the aerosol sample flow leaving the DMA was conducted to the first CPC, where the particle concentration of the monodisperse aerosol was determined, whereas the other half was humidified to a defined RH before entering the second DMA. The second DMA scanned an interval of the humidified particle size distribution and worked in combination with the second CPC as a size spectrometer to determine the hygroscopic growth factors and number fractions of individual hygroscopic growth groups that occurred in the spectra. The H-TDMA system was operated at 90%

ACPD
10, 25991–26044, 2010

RH and at initial dry diameters of $D_p = 30, 50, 80, 150, 250$ and 350 nm. A complete cycle of six spectra at 90% RH took approximately one hour including a calibration scan with sodium chloride particles at $D_p = 100$ nm to recalculate the RH in the second DMA. Before proceeding the data analysis, the quality of the data was checked. Particularly, a fluctuation was tolerated in the H-TDMA system of ± 1% in relative humidity and ± 1% in flow rates during one scan. Moreover, scans with instable concentrations in the first CPC and incorrect measurements from the second CPC were excluded from further data analysis.

2.4 Coarse particle hygroscopicity (H-DMA-APS)

The hygroscopic properties of coarse particles were analyzed using a Hygroscopicity Differential Mobility Analyser-Aerodynamic Particle Sizer system (H-DMA-APS). Details of this instrument have been reported in Leinert and Wiedensohler (2008). Briefly, the H-DMA-APS consists of a High Aerosol Flow DMA (HAF-DMA) and two additional APS instruments (model 3320, TSI Inc.). The HAF-DMA is a custom-built DMA, which was operated at an aerosol flow of 2 l min^{-1} and a sheath air flow of 20 l min^{-1}. Downstream of the HAF-DMA the sample flow was divided into two parts. One part was supplied to the first APS, measuring the particle number size distribution at dry conditions (RH < 10%), and the other part was conditioned to a certain, defined RH before being analyzed by the second APS at this RH. Thus, with the first APS the number size distribution downstream of the HAF-DMA in dry state was determined and with the second APS the humidified number size distribution of the monodisperse aerosol at defined conditions was measured. For this reason, the sheath air of the second APS was conditioned to the same RH as the sampled and humidified aerosol. The H-DMA-APS system was used to determine the hygroscopic growth of particles at dry mobility diameters 1.0 and 1.2 µm. One measurement required between 15 and 30 min, depending on the available ambient particle concentration. Every four hours a calibration scan was carried out using polystyrene particles ($D_p = 1.05$ µm) to verify drifts related to particle sizing.

ACPD
10, 25991–26044, 2010

The quality check of the H-DMA-APS included also an inspection of the relative humidity and the determination of the Poisson error of the APS counts. The presented H-DMA-APS results are averaged over 12 h in order to achieve statistically robust results. The flow rates and the relative humidities fluctuated during one scan in a range of ±2–3%. This higher fluctuation in comparison to the H-TDMA is caused by the longer sampling time for this instrument. An uncertainty of 2% in RH leads to a 6–10% theoretical uncertainty in all determined growth factors.

2.5 Aerosol optical scattering and absorption

The total and backscattering coefficients ($\sigma_{sp,neph}$ and $\sigma_{bsp,neph}$, respectively) were measured at dry conditions with a three-wavelength, and total/backscatter nephelometer (model 3563, TSI Inc.) at wavelengths of 450, 550 and 700 nm. Design and applications of the instrument were summarized in Heintzenberg and Charlson (1996). Calibrations were carried out with filtered particle-free air as the low span gas and CO_2 as the high span gas (Anderson and Ogren, 1998). Zero baseline checks were performed at least once a week. The absolute uncertainty of the measured $\sigma_{sp,neph}$ and $\sigma_{bsp,neph}$ were estimated to be 7% (Anderson et al., 1996).

A Multi-Angle Absorption Photometer (MAAP model 5012, Thermo Inc., Waltham, USA) was used to measure the aerosol light absorption coefficient ($\sigma_{ap,MAAP}$) at a wavelength of 637 nm[1] under dry conditions. The MAAP determines aerosol light absorption from the simultaneous measurements of radiation passing through and scattered back from particles accumulating on a filter tape. It operates at three detection angles to resolve the influence of light-scattering aerosol components on the angular distribution of the back scattered radiation (Petzold and Schönlinner, 2004). The flow rate was calibrated once per week using a bubble flow meter. Using a specific attenuation cross section of 6.6 $m^2\,g^{-1}$ the MAAP converts the light absorption signal into a mass

[1]Note that the manufacturer specifies a wavelenghth of 670 nm. Experimental verification of the wavelength in the laboratory, hovewer, yielded a value of 637 nm (Müller et al., 2010).

ACPD
10, 25991–26044, 2010

concentration of black carbon (soot). The absolute measurement uncertainty of the MAAP was determined to be 12% (Petzold and Schönlinner, 2004) while laboratory intercomparisons of multiple MAAP instruments suggested a unit-to-unit variability below 3% (Müller et al., 2010).

2.6 Chemical composition

Aerosol samples for subsequent chemical analysis were collected using a Small Deposit Area Low Volume-Impactor (SDI; Maenhaut et al., 1996). The upper cut-off size of the device was 10 µm, with 12 collection stages being provided between 0.041 and 10 µm. During ARIADNE the average sampling period was 48 hours at a flow rate of 20 l min^{-1}. The filters were covered by aluminium foil, sealed in polyethylene bags and stored in a refrigerator at 4 ° C prior to analysis. Chemical analysis yielded inorganic ions as well as elemental carbon (EC) and particulate organic matter (POM). For technical details of the analytical procedures we refer the reader to Teinilä et al. (2000).

3 Methods

3.1 Processing of hycroscopicity data

3.1.1 H-TDMA: volume equivalent growth factors and number fractions

Gaussian distributions were fitted to the particle number size distribution recorded downstream of the humidification step. On the basis of their modal mean diameters and particle numbers, wet particle growth factors and their corresponding number fractions were determined for each hygroscopic particle mode.

The volume equivalent growth factors gf_{ve} were calculated for sub-micrometer sizes (30–350 nm) measured with the H-TDMA from the ratio of the wet particle diameter and the dry particle diameter (see Eq. 1) (DeCarlo et al., 2004).

ACPD
10, 25991–26044, 2010

$$gf_{ve} = \frac{D_{p,wet(ve)}}{D_{p,dry(ve)}} \quad (1)$$

Sodium chloride calibration scans carried out at at 90% RH were used to determine the real RH inside the second DMA. Based on this calculation the growth factors measured with the H-TDMA were recalculated using a solubility model (see Sect. 3.2 below) to a standard RH of 90%. The number fraction nf represents the ratio of the number of particles belonging to one hygroscopic growth group and the sum of the particles of all groups (see Eq. 2). Here, the index *i* declares the number of the group.

$$nf = \frac{nf_i}{\sum_{i=1}^{3} nf_i} \quad (2)$$

3.1.2 H-DMA-APS: aerodynamic growth factors and number fractions

The characteristics of the measured humidified size distributions differed between the H-TDMA and the H-DMA-APS. The dry size distribution measured with the first APS of the H-DMA-APS showed a bimodal and sometimes a trimodal behavior. The reason was the combination of the different measurement principles of DMA and APS. Larger particles with multiple charges were observed as a small mode right of the main peak in the particle number size distribution measured with the dry APS. Therefore this mode was not used for the determination of hygroscopic growth. Small hydrophobic particles with higher shape factors and the same electrical mobility as the particles of the main peak appeared in the dry particle number size distribution left to the main peak. The same group of hydrophobic particles was found in the wet particle number size distributions. The parameters of the left mode and the main mode were used to determine the aerodynamic growth factors and their corresponding number fractions of different hygroscopic growth groups measured with the H-DMA-APS system. The calculation of the aerodynamic growth factors and number fractions follows the Eqs. (1) and (2) for the H-TDMA, but the used diameters are aerodynamic, therefore the determined growth factors are aerodynamic growth factors.

ACPD
10, 25991–26044, 2010

3.2 Solubility model

A simplistic solubility model was used to calculate the soluble volume fraction of the particles from the recalculated growth factors at 90% RH (H-TDMA) and 85% RH (H-DMA-APS), respectively. The used solubility model is based on the assumption, that the measured particles consist of an insoluble core coated by soluble material. The soluble volume fraction was estimated by Swietlicki et al. (1999) as:

$$\varepsilon_{(\mathrm{RH})} = \frac{\mathrm{gf}^3_{\mathrm{measured(RH)}} - 1}{\mathrm{gf}^3_{\mathrm{theoretical(RH)}} - 1} \tag{3}$$

The theoretical growth factor $\mathrm{gf}_{\mathrm{theoretical}}$ is determined by the hygroscopic growth of a theoretical particle, which is composed of only one soluble component having the same wet diameter as the measured particle at the RH of the individual measurement. Growth factors reported by Tang and Munkelwitz (1994) were used to describe the growth of pure sodium chloride (H-DMA-APS) and pure ammonium sulfate particles (H-TDMA).

Furthermore, the total soluble volume fraction $\varepsilon_{\mathrm{tot}}$ was determined. This parameter considers a theoretical bulk particle and characterizes the mean solubility of one certain particle size taking into account the fractionation into the different hygroscopic growth groups.

$$\varepsilon_{\mathrm{tot}} = \sum_{i=1}^{3} \mathrm{nf}_i \cdot \varepsilon_i \tag{4}$$

The recalculated hygroscopic growth factors $\mathrm{gf}_{\mathrm{ve}}$ at 90% RH of the H-TDMA were averaged over the impactor periods and then transformed to a mean volume hygroscopic growth factor $\mathrm{gf}_{\mathrm{v\text{-}mean}}$ for the measured particle diameters, to compare them with the results of the chemical growth model $\mathrm{gf}_{\mathrm{chem}}$. The following Eq. (5) describes the calculation of $\mathrm{gf}_{\mathrm{v\text{-}mean}}$.

ACPD
10, 25991–26044, 2010

$$gf_{v\text{-}mean} = \sqrt[3]{\sum_{i=1}^{3} gf_{i,ve}{}^{3} \cdot nf_i} \quad (5)$$

3.3 Optical model

To examine the influence of the particle's hygroscopicity on its light scattering and therewith on the local visibility, an optical model was applied to model the particle optical properties at ambient conditions. The scheme is outlined in Fig. 2. Particles are assumed to grow as a result of their interaction with water vapour. They are assumed to be spherical, so that the homogeneous spherical Mie code can be appiled (Bohren and Huffman, 1998). As illustrated in the right-hand part of Fig. 2, particle number size distributions and complex refractive indices at ambient RH were required as input parameters for the optical model.

3.3.1 Parameterizations of particle hygroscopicity

A central objective of our work was to study the dependency of aerosol optical properties on ambient relative humidity. In order to derive the size-resolved particle hygroscopic growth factors gf(D_p, RH) and particle number size distributions at ambient RH, the required hygroscopic growth model was developed as a hybrid from both, experimental hygroscopicity data and chemical particle analysis from impactor samples collected during the ARIADNE experiment at Finokalia.

For the fine particle mode ($D_p \leq 700$ nm) we derived hygroscopic growth factors from the H-TDMA measurements at 90% RH. The average particle mass size distribution shows a clear bimodal pattern, as presented in Fig. 3. Particle mass was derived by summing up all measured inorganic ions, elemental carbon (EC) and particulate organic matter (POM). Chemical particle analysis of impactor samples suggested that ammonium sulfate constituted the overwhelming fraction of the soluble particulate matter in sub-µm particles in the Eastern Mediterranean aerosol. Thus, a simplistic

ACPD
10, 25991–26044, 2010

hygroscopic growth model was devised, describing particles with $D_p \leq 700$ nm as consisting of an insoluble core coated by ammonium sulfate. Using the experimentally determined growth of ammonium sulfate (Tang and Munkelwitz, 1994) with dependence on RH, the simple two-component model allows estimating the fraction ε of soluble material in the particle at each of the given dry diameters D_p between 30 and 350 nm. The H-TDMA data suggested that for diameters D_p between 50 and 350 nm ε varied between 66% and 74%. Using these soluble volume fractions, the model was applied to calculate the gf(D_p, RH) of particles with D_p between 20 and 700 nm at the corresponding ambient RH.

For the coarse particle mode ($D_p \geq 1.3$ µm) a hygroscopic growth model based on experimental chemical composition was applied. Figure 3 suggested that the chemical composition of super-µm particles was dominated by fresh and processed sea-salt particles (e.g., sodium chloride and nitrate). Accordingly, a three-component model was devised combining an insoluble fraction (supposedly dust) with two soluble fractions of sodium nitrate and sodium chloride, respectively. The growth of the soluble species was again based on experimental data (Tang and Munkelwitz, 1994), with both solutes acting like in an ideally mixed solution (Zdanovskii, 1948; Stokes and Robinson, 1966). The described model was used to calculate the gf(D_p, RH) of particles in the mobility diameter range 1.3–10 µm at prevailing ambient RH. For the intermediate D_p range 700–1300 nm both models were interpolated to provide a smooth transition between the fine and coarse particle modes. On the basis of these parameterizations of the particles' hygroscopicity, gf(D_p, RH) and dry particle number size distributions were used to calculate particle number size distributions at ambient RH (30–95%, average ~71%).

3.3.2 Optically retrieved refractive index

As illustrated in Fig. 2, the optically derived effective complex refractive index ($\tilde{m}_{dry}(n_r, n_i)$) of the aerosol particles at dry conditions was determined by iterative Mie calculations utilizing the simultaneous measurements of particle number size

ACPD
10, 25991–26044, 2010

distributions, three-wavelength total/hemispheric-back scattering, and one-wavelength absorption coefficients. The approach of the retrieval model was similar to those described in Guyon et al. (2003) and Schkolnik et al. (2007). The Mie code iteratively determined the $\tilde{m}_{\mathrm{dry}}$ for a given particle number size distribution by matching the calculated and measured scattering and absorption coefficients (σ_j^c and σ_j^e, respectively, and $j = 1,\ldots,7$ referring to the seven measured optical parameters), as described by Eq. (6). Here, n_{r} and n_i were the real and imaginary parts of $\tilde{m}_{\mathrm{dry}}$, respectively. The code assumed spherical particles and homogeneous, internally mixed particle compositions.

$$\underset{n_{\mathrm{r}},n_i}{\text{Minimize}}\ \chi^2(n_{\mathrm{r}},n_i) = \sum_{j=1}^{7}\left|\frac{\sigma_j^c-\sigma_j^e}{\sigma_j^e}\right|^2 \tag{6}$$

The minimization was achieved by a Newton-Raphson Iterative Method (Press et al., 1992). The partial derivatives of $\chi^2(n_{\mathrm{r}},n_i)$ with respect to n_{r} and n_i vanished when $\chi^2(n_{\mathrm{r}},n_i)$ approached the minimum value. Δn_{r} and Δn_i were given by:

$$\begin{bmatrix}\Delta n_{\mathrm{r}}\\ \Delta n_i\end{bmatrix} = -J^{-1}\begin{bmatrix}\partial\chi^2/\partial n_{\mathrm{r}}\\ \partial\chi^2/\partial n_i\end{bmatrix}, \tag{7}$$

where J was the Jacobian Matrix (Press et al., 1992).

The value of $\sqrt{(\Delta n_{\mathrm{r}})^2+(\Delta n_i)^2}$ was chosen for stopping threshold, i.e. the iteration converged on condition of $\sqrt{(\Delta n_{\mathrm{r}})^2+(\Delta n_i)^2} < \mathrm{eps}$. Here, eps was set as 10^{-7}.

A sensitivity study was carried out to test whether a unique solution can be achieved for the current data set. A series of refractive indices was assumed to vary from 1.33 to 1.70 for n_{r} and from 0 to 0.1 for n_i with respect to the expected range of refractive indices of atmospheric aerosol particles. Together with the average particle number size distribution measured at the Finokalia site, they were used to simulate a series of particle optical properties with the homogeneous spherical Mie model (Cheng et al.,

ACPD
10, 25991–26044, 2010

2006). The theoretically calculated optical properties and the averaged particle number size distribution again served as input parameters for the retrieving model. First, the assumed refractive indices could successfully be retrieved. Second, a rough step-search was utilized with a step of 0.05 for n_r and 0.005 for n_i within the range of 1.0 to 2.0 and 0 to 0.2, respectively. Contour plots of the differences between the calculated optical properties and theoretically predicted values showed that there was only one unique solution (trough) in the expected ranges of n_r and n_i. Guyon et al. (2003) also found that the iterative calculations always converged toward a unique solution within the range of refractive indices open to the model, except for very little unusual cases. Thus, the interactive method was capable to provide the desired results for the ARIADNE data set.

A Monte Carlo simulation (Wex, 2002; Cheng et al., 2006) was carried out by randomly (and simultaneously) varying all input parameters (scattering, absorption coefficients and particle number size distribution) in the retrieving model to investigate the uncertainties of retrieved $\widetilde{m}_{dry}$ due to the uncertainties in the experiments. The uncertainties of the retrieval were found to be 5% for n_r and 10% for n_i, which were consistent with Guyon et al. (2003). However, we admit that uncertainties introduced by the assumptions in the model – including the spherical shape and homogeneously internally mixed assumptions for the particles as well as the non-size dependent assumptions for the retrieved $\widetilde{m}_{dry}$, were not taken into account in the uncertainty analysis. We felt that the computational consideration of any particle morphology other than a homogeneous mixture is outside the scope of this work.

In the next step, the retrieved refractive index at dry conditions and the particle's hygroscopic growth factors gf(D_p,RH) were used to calculate the refractive indices of particles at ambient RH (see Fig. 2). At each size bin, the up-taken water volume ratio ($R_{w,V}(D_p,\mathrm{RH})$), defined as the volume ratio of up-taken water and the total particle at ambient RH was determined as $R_{w,V}(D_p,\mathrm{RH}) = \left[\mathrm{gf}(D_p,\mathrm{RH})^3 - 1\right] / \mathrm{gf}(D_p,\mathrm{RH})^3$.

Together with the retrieved $\widetilde{m}_{dry}$ at dry conditions, the $R_{w,V}(D_p,\mathrm{RH})$ were further used to calculate the complex refractive index of each size bin at ambient conditions

ACPD
10, 25991–26044, 2010

($\tilde{m}(D_p, \mathrm{RH})$), according to a simple volume mixing rule (Covert et al., 1972). The refractive index of water was used as 1.33–0i.

4 Results and discussion

4.1 Campaign overview and air mass classification

Among all measured aerosol and gas phase parameters, the mass concentration of soot turned out to be the most favourable indicator for the anthropogenic influence on the air masses sampled during ARIADNE. Figure 4 shows the time series of the soot mass concentration, the relative mass fraction of soot, and particle mass concentration of particles $< 1\,\mu$m. Four distinct time periods (A1–A4) were defined, representing low (A1, A3) and high (A2, A4) mass concentrations of soot. These four periods coincide with the episodes of low and high total particle mass as well as accumulation mode particle number (see Fig. 4), and are identical to those defined in (Kalivitis et al., 2008). The latter reference also presents particle number size distributions corresponding to the four periods. The four periods are listed in Table 1.

The air masses during A1 and A3 originated in the Western Mediterranean Sea (cf. back trajectories in Fig. 5), and showed only minor continental influence. Consequently, they are termed "marine" air masses in the following. The counterpart are the periods A2 and A4, during which the back trajectories pointed to continental source regions on the north-eastern shore of the Mediterranean (see Fig. 5). The soot and total particle mass concentrations showed higher levels compared to A1 and A3 and are therefore described as "continentally polluted" hereafter.

A look at the size-fractionated chemical composition of the particles confirmed a systematic difference between fine and coarse particles: Fine particles consist overwhelmingly of ammonium sulphate and organic matter, coarse particles of sodium chloride and nitrate (see Fig. 6). Soot occurs in minor mass fractions between 2 and 6% only, as already shown in Fig. 3. The continentally influenced aerosol (A4) is distinguished from the rather marine aerosol (A1) by an elevated fraction of organic matter.

ACPD
10, 25991–26044, 2010

4.2 Particle hygroscopicity

4.2.1 Hygroscopic growth factors and soluble volume fractions

The measurements of both hygroscopicity instruments revealed three groups of particles with different hygroscopic behavior. These particle groups were differentiated in a "more hygroscopic" group, a "less hygroscopic" and a "nearly hydrophobic" particle group. This finding is in broad agreement with the compilation of previous H-TDMA observations (Swietlicki et al., 2008).

The hygroscopicity of fine particles was derived from the H-TDMA. Table 2 compiles the mean hygroscopic growth factors, their corresponding number fractions, soluble volume fractions and total soluble volume fractions with their standard deviations. Ammonium sulfate was assumed as the dominant soluble material for the calculation of soluble volume fractions of sub-micrometer particles independent on hygroscopic growth group (see Sect. 3.2) with respect to the observed chemical composition. These assumption is consistent with the chemical composition presented in Fig. 6. This Figure displays the percentage mass fractions of analyzed ions during the time periods A1 (marine) and A4 (continentally-polluted) for the fine ($D_p < 1\,\mu m$) and coarse ($D_p > 1\,\mu m$) particle fractions. Obviously, the major ions were SO_4^{2-}, NH_4^+, NO_3^-, Cl^- and Na^+. This is in a good agreement with an earlier experiment in this area (Bardouki et al., 2003).

The hygroscopicity of coarse particles was assessed using the H-DMA-APS instrument. Because of the poor counting statistics of the H-DMA-APS measurements, yielding long integration times, a segregation of the data into the four classified air masses (A1–A4) was impossible. Instead, only mean values of the particle number fractions and aerodynamic growth factors are listed in Table 3.

In fact the hygroscopic growth factor of the more hygroscopic particle group increased with an increasing particle diameter (see Table 2). Furthermore, the number fraction of the more hygroscopic particles was about 80% in the sub-micrometer range and decreased to about 40% in the super-micrometer range ($D_p = 1.2\,\mu m$, see

ACPD
10, 25991–26044, 2010

Table 3). It has to be pointed out that the number fraction of the nearly hydrophobic particle group started to increase from about 10% in the sub-micrometer range at $D_p = 250$ nm to about 30% at $D_p = 1.2$ µm. While the mass in the fine particle fraction was clearly dominated by sulfate, the coarse fraction showed notable number contributions of insoluble particles, most likely dust particles.

4.2.2 Relationship between hygroscopicity and soot

In Fig. 7 the total soluble volume fraction, determined from H-TDMA measurements, is compared against the mass fraction of EC for the four defined air masses A1–A4. The lowest correlation coefficients were found for fine particles with diameters of 30 and 50 nm. In contrast, 150 nm particles had the highest R^2 value of 0.74. This originates in the characteristic maximum of the soot number size distribution, which resides between 50 and 100 nm. However, particles reaching the Finokalia measurement site were usually not directly freshly emitted but may originate from continental sources and be transformed by atmospheric condensation processes. Thus, the highest correlation between insoluble particle volume and soot fraction was found for larger particles with $D_p = 100$ nm indicating the highest soot fraction. This result agrees well with the average size distribution for elemental carbon (EC) retrieved from the size segregated chemical analysis which is centered around $D_p = 130$ nm (see Fig. 8). The density of EC was estimated to be 1.9 g cm^{-3} (Fuller et al., 1999), which is necessary for the conversion of mass size to number size distributions.

The clear dependence of the total soluble volume fraction on the soot fraction is also visible in Fig. 9. The total soluble volume fraction increased during the marine periods with increasing dry diameter for sub-micrometer aerosol. In general, the total soluble volume fraction decreased with increasing relative soot fraction. This effect is strongest for accumulation mode particles ($D_p = 150$, 250, and 350 nm).

It is noticeable from Fig. 9 that during the polluted time period, the soluble volume fraction is rather insensitive on particle diameter. The lower soluble volume fraction is

ACPD
10, 25991–26044, 2010

also consistent with the increased amounts of organic matter (see Fig. 6). The soluble volume fractions of 30 nm show the lowest overall values, regardless of air mass type. This is suggestive of their physico-chemical properties being less influenced by long-range transport, and points to local sources or atmospheric secondary formation as the responsible source processes.

4.3 Amplification of aerosol scattering

4.3.1 Optical model initialization: retrieved refractive index at dry conditions

As described in Sect. 3.3 and illustrated in Fig. 2, effective refractive indices of aerosol particles at dry conditions were one of the key parameters to initialize the optical simulations at ambient RH. The $\tilde{m}_{\mathrm{dry}}(n_{\mathrm{r}}, n_i)$ were retrieved by the iterative Mie calculations using the best fit between the measured aerosol optical properties and the calculated ones. Table 4 shows correlations between the seven calculated and measured optical properties (σ_j^c and σ_j^e) with slope (b) and correlation coefficients (R^2). The linear fitting was done to match zero. Excellent agreement between σ_{ap}^c and σ_{ap}^e has been found with b of 0.99 and R^2 nearly 1.0. In general, the simulated and measured scattering coefficients followed each other very well. Also, all correlation coefficients R^2 were found to be greater than ~0.95. Except for $D_{\mathrm{p}} = 700$ nm, the deviations between the measured and calculated total/hemispheric back scattering coefficients were less than ~7%. Larger deviations occurred at 700 nm. However, intercomparison studies of nephelometers in the laboratory also indicate that there might be higher uncertainties in the measured light scattering at $D_{\mathrm{p}} = 700$ nm (Heintzenberg et al., 2006). On the basis of the comparison between the calculated and measured optical properties, it could be concluded that the retrieving model was suitable to provide time series of the refractive index and in general the retrieved $\tilde{m}_{\mathrm{dry}}(n_{\mathrm{r}}, n_i)$ were capable to well represent the measured particle scattering and absorption coefficients at dry conditions.

ACPD
10, 25991–26044, 2010

During the field study, different air masses were observed and they were classified with respect to their origin based on air mass back trajectory analysis (see Sect. 4.1). In particular, air masses of marine origin from the Mediterranean Sea and those strongly imprinted by continental contact with South-East Europe were observed. According to Table 1, particle optical properties and retrieved refractive indices at dry conditions were also classified into two groups, marine (m) and continentally-polluted (cp) periods. Figure 10 presents time series of the total scattering coefficient at 550 nm ($\sigma_{sp,neph,550\,nm}$) and absorption coefficient at 630 nm ($\sigma_{ap,MAAP,630\,nm}$) measured by the nephelometer and the MAAP, as well as the retrieved n_r and n_i. More detailed statistic information for these parameters during the two different periods were summarized in Table 5.

As shown in Fig. 10, the measured scattering and absorption coefficients generally show a parallel time evolution. However, the respective values were significantly lower for marine air masses (see Fig. 10 and Table 5) compared to the measured ones during the continentally-polluted periods. This was mainly due to the lower mass concentrations of sub-µm particles measured during the marine periods. Real parts of the retrieved refractive indices were very similar for both air mass types (marine ~1.48 and continentally-polluted ~1.50), whereas the average imaginary part was a factor of 2 lower for marine air masses (see Table 5). The real and imaginary parts of refractive index were highly variable for marine air masses, probably due to individual emission sources (e.g., ships).

4.3.2 Optical simulation at ambient RH: influence of particle hygroscopicity on light scattering

In order to investigate the influence of the particle's hygroscopicity on light scattering for the Eastern Mediterranean aerosol, two cases were chosen: the marine air mass A1 (23–25 September 2005) and the continentally-polluted air mass A4 (6–9 October 2005) (see Table 1). With the methods introduced in Sect. 3.3, average particle hygroscopic growth factors of marine and continentally-polluted periods were respectively

ACPD
10, 25991–26044, 2010

applied to these two cases. Figure 11 presents the time series of the calculated aerosol scattering coefficient at $\lambda = 550$ nm at ambient RH together with the measured values by the nephelometer at dry conditions.

In addition, the relative humidity and the scattering growth factor (scattering coefficient at ambient conditions divided by that at dry conditions, $\xi_{sp}(RH) = \sigma_{sp,amb}/\sigma_{sp,dry}$) for both marine and continentally-polluted cases are shown. The truncation of the nephelometer was taken into account in the optical simulations. Data gaps during the continentally-polluted period were due to missing data of the measured aerosol optical properties. Pronounced enhancement of particle scattering due to particle hygroscopicity was found during both, the marine and the continentally-polluted cases (see Fig. 11a). The ξ_{sp} basically followed the pattern of RH (see Fig. 11b).

In Fig. 12, the ξ_{sp} are plotted as a function of RH for both cases. When the marine air masses dominated at Finokalia, the $\xi_{sp}(80\%)$ ranged from 2.7 to 3.5. This is consistent with the measured scattering growth factor at RH 80% for sea salt and $(NH_4)_2SO_4$ (3.4 and 2.2, respectively) (Covert et al., 1972), since the aerosol composition was dominated by sea salt particles combined with some fractions of ammonium sulfate. In marine air the aerosol scattering coefficient varied with RH as theoretically expected from sea salt particles. However, it is worth noticing that $\xi_{sp}(80\%)$ for the marine case at Finokalia station was higher than the values of clean marine aerosols (1.8–2.5) reported by previous studies at other locations. For example, the reported $\xi_{sp}(80\%)$ for clean marine periods at Cape Grim, Tasmania were 2.0 ± 0.2 and 2.5 ± 0.2 (measured using a humidified nephelometer; Carrico et al., 1998) and the respective values were on average 2 in Seattle (Covert et al., 1972), 2.09 off the mid-Atlantic coast of the United States (Kotchenruther et al., 1999), and 2.3 ± 0.3 in clean marine air near the coast of California and Washington. Moreover, for higher RH during the marine case at Finokalia, the simulated amplification of scattering due to particle water uptake could be as large as a factor of 5 at RH 90% and 7 to 8 at RH ~95%.

Compared to the clean marine case, the chemical particle composition during the continentally-polluted periods at the Finokalia site consisted of a relatively more

ACPD
10, 25991–26044, 2010

complicated mixture of various chemical compounds and also the variation in particle number size distribution was higher. Referring to Fig. 12, the differences in ξ_{sp} between marine and continentally-polluted cases are significant. The scattering growth factors during the continentally-polluted case were always much smaller than those during the marine case, regardless of the variation of RH. Also, the amplification rate of scattering with increasing RH during the continentally-polluted case was lower than that during the marine case. At RH 90%, the ξ_{sp} during continentally-polluted periods was less than 3 (see the zoom-in subset in Fig. 12), whereas the respective growth during the marine period reached up to about a factor of 5. A strong enhancement of particle scattering due to water uptake at RH > 90% was observed in marine-type air; unfortunately, no case of similarly high RH was observed during ARIADNE in polluted air that could serve for a direct comparison.

Based on a comparison of existing studies $\xi_{sp}(80-85\%)$ can be concluded change with time, space, and aerosol type (Covert et al., 1972; Sloane and Wolff, 1985; Malm et al., 1994; Hegg et al., 1996; Tang, 1996; Li-Jones et al., 1998; Kotchenruther and Hobbs, 1998; Kotchenruther et al., 1999; Gassó et al., 2000; Koloutsou-Vakakis et al., 2001; Im et al., 2001; Hegg et al., 2002; Sheridan et al., 2002; Randriamiarisoa et al., 2006; Bundke et al., 2002; Nessler et al., 2005; Raut and Chazette, 2007; Cheng et al., 2008). The reported literature values range from 1.8 to 2.5 for clean marine aerosols, 1.58 to 1.81 for polluted marine aerosols, 1.4 to 1.65 for anthropogenic aerosols, ~1.0 to 1.13 for dust aerosols and ~1.1 to 1.4 for fresh biomass burning particles. As global average, 1.7 ± 0.3 was used by Charlson et al. (1991) for anthropogenic sulfate aerosols in a 3-dimensional global model. Our results for the continentally-polluted case were found to be higher than those reported for polluted marine aerosols and anthropogenic aerosols in other studies. This may indicate a relatively significant influence of marine aerosols during the continentally-polluted period.

As the respective average size-segregated hygroscopic growth law was applied overall to individual cases (marine or continentally-polluted cases), we would like to evaluate the influence of the dry particle number size distributions on the particle scattering

ACPD
10, 25991–26044, 2010

growth. Thus, the effective diameter ($D_{p,eff}$) of fine particle number size distributions (< 1 µm) at dry conditions was calculated as

$$D_{p,eff} = \int (D_p)^3 \cdot n(\log D_p) \cdot d\log D_p \Big/ \int (D_p)^2 \cdot n(\log D_p) \cdot d\log D_p. \quad (8)$$

Here D_p is the particle diameter and $n(\log D_p)$ is the particle number size distribution. As illustrated in Fig. 13, the most efficient scattering amplification in terms of the maximums of ξ_{sp} occurred when the particle effective diameter (< 1 µm) was between 250 and 280 nm when the RH was below 80% for the marine case. If the RH was higher than 80%, the scattering coefficient of particles with smaller $D_{p,eff}$ (220–230 nm) grew effectively too. The pattern of scattering growth factors during the continentally-polluted case was relatively more complex than that of the marine case. However, this might be owing to the smaller number of data points and the smoothing method. The most effective scattering amplification occurred at effective diameters between 260 and 300 nm. A similar behavior of particles with smaller $D_{p,eff}$ (240–260 nm) has also been found during the continentally-polluted case. Tang (1996) investigated the size-effects of hygroscopic behavior on σ_{sp} with numerical methods. They found that assuming the same standard deviation of particle number size distributions, the increase of σ_{sp} with RH was smaller for the particles with a mean geometric diameter of 0.6 µm compared to that for particles with a geometric mean diameter of 0.3 µm. Nessler et al. (2005) also stated that due to the particle size dependence of σ_{sp}, the humidity effect on σ_{sp} was more intense for the smaller particles within the mid-visible λ range.

Our results suggest that at under typical daytime RH at Finokalia (70–80%), a significant fraction of up to ~50–70%) of the visibility degradation (as assessed by light extinction) is caused by the uptake of water by the particles compared to the dry particle state.

ACPD
10, 25991–26044, 2010

4.4 Comparison of aerosol radiative forcing for marine and continentally influenced air masses

In order to estimate and compare the aerosol radiative forcings (ΔF_r) caused by the aerosol in the different air masses under study, a simplistic two-layer-single-wavelength radiative transfer model was used (Chýlek and Wong, 1995). According to this model,

$$\Delta F_r = -\frac{1}{2} S_0 [T_{atm}^2 (1 - A_C)][(1 - R_s)^2 \overline{\beta} \tau_{sp} - 2R_s \tau_{ap}]. \quad (9)$$

Concretely, the factor $\frac{1}{2}$ accounts for the partial length of the day, $S_0 = 1370\,W\,m^{-2}$ is the solar constant, T_{atm} the transmittance of the atmosphere above the aerosol layer with a global average of ~0.76, A_C the fraction of sky covered by clouds, R_s the surface albedo of the underlying ground, τ_{sp} and τ_{ap} are the optical thicknesses of the aerosol layer due to light scattering and absorption, respectively, and $\overline{\beta}$ is the average upscatter fraction.

Finokalia is located on the island Crete in the Eastern Mediterranean Sea, to the south of continental Greece (Fig. 1). For the open Aegean Sea in this region, an average planetary boundary layer (PBL) height of 400 m is typically reported for this time of the year (Kallos et al., 1998). Vardavas and Taylor (2007) indicated that the sea albedo depends on the solar zenith angle (Fresnel reflection), and whether or not the sky is cloudy. For cloudy sky (diffuse radiation), the authors report the sea albedo to be about 0.055, for clear sky for overhead sun about 0.021 climbing up to about 0.8 when the sun is low on the horizon. However, for a rough water surface it does not go beyond 0.3 (Vardavas and Taylor, 2007). A mean value of 0.06 was chosen in the model simulations of the present study. The radiative cloud fraction images retrieved from OMI (Ozone Monitoring Instrument) satellite observations (data retrieved from (http://toms.gsfc.nasa.gov/reflect/reflect_v8.html) were checked for the August to October period of 2005. It was confirmed that there were almost no clouds over the Aegean Sea most of the time. Less than 20% of the days showed thin and

ACPD
10, 25991–26044, 2010

only partial cloud covers over the open Aegean sea. So the A_C could be safely set to 0.0 in the radiative calculations.

Wiscombe and Grams (1976) and Marshall et al. (1995) investigated relationships between the asymmetry parameter g and $\overline{\beta}$. For the Mie simulation of the aerosol scattering and absorption at ambient conditions, g was also calculated for the particles at ambient conditions. $\overline{\beta}$(RH) were therefore calculated with g_{amb} at 550 nm by using the Henyey-Greenstein phase function (Wiscombe and Grams, 1976).

The calculated time series of the aerosol single scattering albedo $\omega_{0,550\,nm,amb}$ (= $\sigma_{sp,550\,nm,amb}/(\sigma_{sp,550nm,amb} + \sigma_{ap,550nm,amb})$) and the uperscatter fraction ($\overline{\beta}_{550nm,amb}$) at ambient conditions for both marine and continentally polluted cases are presented in Fig. 14. The average ambient $\omega_{0,550nm}$ was generally higher during the marine period ($\sim 0.97 \pm 0.01$) compared to the continentally polluted period ($\sim 0.94 \pm 0.01$). As the particles grow with increasing RH, the forward scattering increases too, which means that the back scattering and upscatter fraction decrease (Cheng et al., 2008). During marine periods, when the RH reached up to 92% (see Fig. 11), $\overline{\beta}$ dropped down from ~ 0.23 to 0.18. The average values of $\overline{\beta}$ for marine and continentally polluted periods were comparable ($\sim 0.21 \pm 0.02$ and 0.21 ± 0.01, respectively).

To estimate the aerosol direct radiative forcing an assumption was made that the aerosol particles were mixed homogenously within the PBL during daytime of the studied period at the open Aegean Sea between Crete and continental Greece. Accordingly, the calculated aerosol scattering and absorption coefficients at ambient conditions were simply integrated along the PBL height to retrieve ξ_{sp}(RH) and ξ_{ap}(RH). Figure 15 shows the calculated aerosol direct radiative forcing (ΔF_r) during marine and continentally polluted periods based on our simulations. The aerosol direct radiative forcings during both periods were negative indicating a net "cooling" effect. Most of the time, the strength of forcing was dominated by the aerosol load, i.e. the higher the aerosol concentration, the stronger the forcing. ΔF_r of continentally polluted aerosols was most of the time stronger compared to that of marine aerosols (ca. −4 versus

ACPD
10, 25991–26044, 2010

$-1.5\,\mathrm{W\,m^{-2}}$). The ΔF_r shows an anticorrelation with ambient RH during the marine period (the higher the RH, the stronger the forcing), whereas the respective pattern between ΔF_r and RH was not as clear during the continentally polluted period, when the variation was mainly dominated by the changing aerosol concentration. This result is supported by the fact that marine aerosols are suspected to be highly hygroscopic compared to continental anthropogenic aerosols. When RH reached 90% and more at the end of period A1, the ΔF_r intensified to the same level as during continentally polluted periods (ca. $-4\,\mathrm{W\,m^{-2}}$) or even stronger (ca. $-7\,\mathrm{W\,m^{-2}}$). It is worthwhile to note that another general reason for the remarkable negative forcings is the poorly absorbing nature of the particles, manifested by the low overall BC concentrations.

5 Conclusions

This paper presents physical and chemical parameters of aerosol particles collected between August and October 2005 in Finokalia on the northern coast of Crete, Greece. The central goal was to quantify the hygroscopic growth of atmospheric aerosol particles over the Eastern Mediterranean and assess its potential influence on particle light scattering at ambient relative humidty. The H-TDMA and H-DMA-APS instruments revealed the presence of three different hygroscopic particle groups both in the fine and coarse particle modes. At 90% relative humidity, the diameter growth factors of the more hygroscopic group ranged between 1.4 and 1.63. These growth factors increased monotonously from the mobility diameter (D_p) 30 nm to 350 nm. The values encountered were within the broad range given by previous world-wide H-TMDA observations (Swietlicki et al., 2008). A substantially lower growth factor was encountered for the more hygroscopic fraction at $D_p = 1.2\,\mu\mathrm{m}$, which rules out sea salt as the only component present at this particle diameter.

The measurement period was separated into four consecutive time periods (A1–A4) based on air mass origin and the soot mass fraction measured by a MAAP instrument. The two clean marine air masses (A1 and A3) originated in the western Mediterranean

ACPD
10, 25991–26044, 2010

Sea while the two continentally-polluted air masses (A2 and A4) had passed over southeastern Europe and the Black Sea. The differences between these air masses could be clearly seen in the H-TMDA data. Clean marine air masses showed higher values of soluble particle volume fraction (about 80%) than continentally-influenced air masses (60%) in accumulation mode range. These differences in hygroscopicity parameters were supported by differences in chemical particle composition (more organic matter in continentally-influenced air), as determined from impactor samples.

In the second part of our study, the measured particle hygroscopic growth factors were used to simulate aerosol light scattering at ambient conditions. Generally, a pronounced enhancement of particle light scattering due to the particle's hygroscopic water uptake was found both for the marine and continentally-polluted cases. When the marine air masses dominated at Finokalia, the scattering enhancement factor ξ_{sp} (80%) ranged between 2.7 and 3.5, close to the values anticipated for sea-salt particles. At extremely high RH, the simulated amplification of scattering due to water uptake during the marine periods was calculated to be as large as a factor of 5 at RH 90% and 7 to 8 at RH ~95%.

Still, the differences in ξ_{sp} between marine and continentally-polluted cases are significant. During the continentally-polluted case the ξ_{sp} were always much smaller than those during the marine case, regardless of the variation in RH. Also, the amplification rate of scattering with increasing RH during the continentally-polluted case was lower than that of the marine case. At RH 90%, the ξ_{sp} during the continentally-polluted period was less than 3, whereas the respective growth during the marine period reached up to about a factor of 5. The ξ_{sp}(80%) for the continentally-polluted case were found to be higher than those reported for polluted marine aerosols and anthropogenic aerosols in other studies. This may indicate a relatively larger influence of marine aerosols even though it was identified as continentally-polluted period. Our results implied that at typical RH during daytime a high fraction of the visibility degradation was due to the water uptake of hygroscopically active material.

ACPD
10, 25991–26044, 2010

The calculated average ambient $\omega_{0;550\,\mathrm{nm}}$ was generally higher during the marine period ($\sim 0.97 \pm 0.01$) compared to the continentally polluted period ($\sim 0.94 \pm 0.01$). During marine periods, when the RH reached up to 92% $\overline{\beta}$ dropped down from ~ 0.23 to 0.18. The estimated aerosol direct radiative forcings during both periods were negative indicating a net "cooling" effect. In general, the strength of forcing was dominated by the aerosol concentration during most of the time, and anti-correlated with ambient RH during the marine period, whereas the respective pattern between ΔF_r and RH was not as clear during the continentally polluted period. Here, the variation was mainly dominated by the variation of aerosol concentrations.

Acknowledgements. This work was supported by the German Academic Exchange Service DAAD (PPP programme with Greece) and Atmospheric Composition Change – The European Network of Excellence (ACCENT). The authors acknowledge the NOAA Air Resources Laboratory (ARL) for the provision of the HYSPLIT transport and dispersion model (http://www.arl.noaa.gov/ready/hysplit4.html) used in this publication. Parts of the data evaluation for this paper were conducted within the European Integrated project on Aerosol Cloud Climate and Air Quality Interactions (EUCAARI), coordinated by the University of Helsinki.

References

Anderson, T. L. and Ogren, J. A.: Determining aerosol radiative properties using the TSI 3563 Integrating Nephelometer, 29, 57–69, 1998. 25998

Anderson, T. L., Covert, D. S., Marshall, S. F., Laucks, M. L., Charlson, R. J., et al.: Performance characteristics of a high-sensitivity, three-wavelength, total scatter/backscatter nephelometer, J. Atmos. Ocean. Technol., 13, 967–986, 1996. 25998

Bardouki, H., Liakakou, H., Economou, C., Sciare, J., Smolik, J., et al.: Chemical compositon of size-resolved atmospheric aerosols in the eastern Mediterranean during summer and winter, Atmos. Env., 37, 195–208, 2003. 26007

Bergin, M. H., Ogren, J. A., Schwartz, S. E., and McInnes, L. M.: Evaporation of ammonium nitrate aerosol in a heated nephelometer: implications for field measurements, Environ. Sci. Technol., 31, 2878–2883, 1997. 25995

ACPD

10, 25991–26044, 2010

Birmili, W., Stratmann, F., and Wiedensohler, A.: Design of a DMA-based size spectrometer for large particle size range and stable operation, J. Aerosol Sci., 30, 549–554, 1999. 25995
Bohren, C. F. and Huffman, D. R.: Absorption and scattering of light by small particles, John Wiley & Sons, Inc., 1998. 26002
Bougiatioti, A., Fountoukis, C., Kalivitis, N., Pandis, S. N., Nenes, A., and Mihalopoulos, N.: Cloud condensation nuclei measurements in the marine boundary layer of the Eastern Mediterranean: CCN closure and droplet growth kinetics, Atmos. Chem. Phys., 9, 7053–7066, doi:10.5194/acp-9-7053-2009, 2009. 25994
Brechtel F. and Kreidenweis S.: Predicting particle critical supersaturation from hygroscopic growth measurements in the humidified TDMA, part I: Theory and sensitivity studies, J. Atmos. Sci, 57, 1854–1871, 2000. 25993
Bundke, U., Hänel, G., Horvath, H., Kaller, W., Seidl, S. et al.: Aerosol optical properties during the Lindenberg Aerosol Characterization Experiement (LACE-98), J. Geophys. Res., 107(D21), 8123, doi:10.1029/2000JD000188, 2002. 26012
Carrico, C. M., Rood, M. J., and Ogren, J. A.: Aerosol light scattering properties at Cape Grim, Tasmania, during the First Aerosol Characterization Experiment (ACE-1), J. Geophys. Res., 103, 16565–16574, 1998. 26011
Carrico, C. M., Bergin, M. H., Xu, J., Baumann, K., and Maring, H.: Urban aerosol radiative properties: measurements during the 1999 Atlanta Supersite Experiment, J. Geophys. Res., 108, 8422, doi:10.1029/2001JD001222, 2003. 25995
Charlson, R. J., Langner, J., Rodhe, H., Leovy, C. B., and Warren, S. G.: Perturbation of the northern heimisphere radiative balance by backscattering from anthropogenic sulfate aerosols, Tellus, 43B, 152–163, 1991. 26012
Cheng, Y., Wiedensohler, A., Eichler, H., Heintzenberg, J., Tesche, M., et al.: Relative humidity dependence of aerosol optical properties and direct radiative forcing in the surface boundary layer at Xinken in Pearl River Delta of China: An observation based numerical study, 42, 6373–6397, 2008. 26012, 26015
Cheng, Y. F., Eichler, H., Wiedensohler, A., Heintzenberg, H., Zhang, Y. H., et al.: Mixing state of elemental carbon and non-light-absorbing aerosol components derived from in situ particle optical properties at Xinken in Pearl River Delta of China, J. Geophys. Res., 111, D20204, doi:10.1029/2005JD006929, 2006. 26004, 26005
Chýlek, P. and Wong, J.: Effect of absorbing aerosols on global radiation buget, Geophys. Res. Lett., 22, 929–931, 1995. 26014

ACPD
10, 25991–26044, 2010

Covert, D. S., Charlson, R. J., and Ahlquist, N. C.: A study of the relationship of chemcial compostion and humidity to light scattering by aerosols, J. Appl. Meteorol., 11, 968–976, 1972. 26006, 26011, 26012

DeCarlo, P., Slowik, J., Worsnop, D., Davidovits, P., and Jimenez, J.: Particle morphology and density characterization by combined mobility and aerodynamic diameter measurements. Part 1: theory, Aerosol Sci. Technol., 38, 1185–1205, 2004. 25999

Fuller, K. A., Malm, W. C., and Kreidenweis, S. M.: Effects of mixing on extinction by carbonaceous particles, J. Geophys. Res., 104, 15941–15954, 1999. 26008

Gassó, S., Hegg, D. A., Covert, D. S., Collins, D., Noone, K., et al.: Influence of humidity on the aerosol scattering coefficient and its effct on the upwelling radiance during ACE-2, Tellus, 52B, 546–567, 2000. 26012

Grant, K. E., Chuang, C. C., Grossman, A. S., and Penner, J. E.: Modeling the spectral optical properties of ammonium sulfate and biomass burning aerosols: Parameterization of relative humidity effects and model results, Atmos. Env., 33, 2603–2620, 1999. 25993

Guyon, P., Boucher, O., Graham B., Beck, J., Mayol-Bracero, O. L. et al.: Refractive index of aerosol particles over the Amazon tropical forest during LBA-EUSTACH 1999, J. Aerosol Sci., 34, 883–907, 2003. 26004, 26005

Gysel, M., Weingartner, E., Nyeki, S., Paulsen, D., Baltensperger, U., Galambos, I., and Kiss, G.: Hygroscopic properties of water-soluble matter and humic-like organics in atmospheric fine aerosol, Atmos. Chem. Phys., 4, 35–50, doi:10.5194/acp-4-35-2004, 2004. 25993

Haywood, J. and Boucher, O.: Estimates of the direct and indirect radiative forcing due to tropospheric aerosols: A review, Rev. Geophys., 38(4), 513–543, 2000. 25993

Hegg, D. A., Covert, D. S., Rood, M. J., and Hobbs, P. V.: Measurements of aerosol optical properties in marine air, J. Geophys. Res., 101, 12893–12903, 1996. 26012

Hegg, D. A., Covert, D. S., and Crahan, K.: The dependence of aerosol light scattering on RH over the Pacific Ocean, Geophys. Res. Lett., 29, 1219, doi:10.1029/2001GL014495, 2002. 26012

Heintzenberg, J. and Charlson, R. J.: Design and applications of the integrating nephelometer: A review, J. Atmos. Ocean. Technol., 13, 987–1000, 1996. 25998

Heintzenberg, J., Wiedensohler, A., Tuch, T. M., Covert, D. S., Sheridan, P., et al.: Intercomparisons and aerosol calibrations of 12 commercial integrating nephelometers of three manufacturers, J. Atmos. Ocean. Technol., 23, 902–914, 2006. 26009

Im, J.-S., Saxena, V. K., and Wenny, B. N.: An assessment of hygroscopic growth factors for

ACPD

10, 25991–26044, 2010

aerosols in the surface boundary layer for computing direct radiative forcing, J. Geophys. Res., 106, 20213–20224, 2001. 26012

IPCC: Contribution of Working Group I to the Fourth Assessment Report of the Intergovernmental Panel on Climate Change, edited by: Solomon, S., Qin, D., Manning, M., Chen, Z., Marquis, M., Averyt, K. B., Tignor, M., and Miller, H. L., Cambridge University Press, Cambridge, United Kingdom, 2007. 25993

Kallos, G., Kotroni, V., Lagouvardos, K., and Papadopoulos, A.: On the long-range transport of air pollutants from Europe to Africa, Geophys. Res. Lett., 25, 619–622, 1998. 26014

Kalivitis, N., Birmili, W., Stock, M., Wehner, B., Massling, A., Wiedensohler, A., Gerasopoulos, E., and Mihalopoulos, N.: Particle size distributions in the Eastern Mediterranean troposphere, Atmos. Chem. Phys., 8, 6729–6738, doi:10.5194/acp-8-6729-2008, 2008. 25994, 26006

Koloutsou-Vakakis, S., Carrico, C. M., Kus, P., Rood, M. J., Li, Z., et al.: Aerosol properties at a midlatitude Northern Hemisphere continental site, J. Geophys. Res., 106, 3019–3032, 2001. 26012

Kotchenruther, R. A. and Hobbs, P. V.: Humidification factors of aerosols from biomass burning in Brazil, J. Geophys. Res., 103, 32081–32090, 1998. 26012

Kotchenruther, R. A., Hobbs, P. V., and Hegg, D. A.: Humidification factors for atmospheric aerosols off the mid-Atlantic coast of the United States, J. Geophys. Res., 104, 2239–2251, 1999. 26011, 26012

Leinert, S. and Wiedensohler, A.: A DMA and APS based technique for measuring aerodynamic hygroscopic growth factors of micrometer-size aerosol particles, J. Aerosol Sci., 39, 393–402, 2008. 25997

Lelieveld, J., Berresheim, H., Borrmann, S., Crutzen, P., Dentener, F., et al.: Global air pollution crossroads over the Mediterranean, Science, 298, 794–799, 2002. 25994

Levy, H. I.: Normal atmosphere: Large radical and formaldehyde concentrations predicted, Science, 173, 141–143, 1971.

Li-Jones, X., Maring, H. B., and Prospero, J. M.: Effect of relative humidity on light scattering by mineral dust aerosol as measured in the marine boundary layer over the tropical Atlantic Ocean, J. Geophys. Res., 103, 31113–31121, 1998. 26012

Maenhaut, W., Hillamo, R., Mäkelä, T., Jafferzo, J.-L., Bergin, M., and Davidson, C.: A new cascade impactor for aerosol sampling with subsequent PIXE analysis, Nucl. Instr. Meth. Phys. Res. B, 109/110, 482–487, 1996. 25999

ACPD

10, 25991–26044, 2010

Malm, W. C., Sisler, J. F., Huffman, D., Eldred, R. A., and Gahill, T. A.: Spatial and seasonal trends in particle concentration and optical extinction in the United Sates, J. Geophys. Res., 99, 1347–1370, 1994. 26012

Marshall, S. F., Covert, D. S., and Charlson, R. J.: Relationship between asymmetry parameter and hemispheric backscatter ratio: Implications for climate forcing by aerosols, AO, 34, 6306–6311, 1995. 26015

Massling, A., Stock, M., and Wiedensohler, W.: Diurnal, weekly, and seasonal variation of hygroscopic properties of submicrometer urban aerosol particles, Atmos. Env., 39, 3911–3922, 2005. 25996

Mihalopoulos, N., Stephanou, E., Kanakidou, M., Pilitsidis, S., and Bousquet, P.: Tropospheric aerosol ionic composition in the Eastern Mediterranean region, Tellus, 49 B, 314–326, 1997. 25995

Müller, T., Henzing, J. S., de Leeuw, G., Wiedensohler, A., Alastuey, A., Angelov, H., Bizjak, M., Collaud Coen, M., Engström, J. E., Gruening, C., Hillamo, R., Hoffer, A., Imre, K., Ivanow, P., Jennings, G., Sun, J. Y., Kalivitis, N., Karlsson, H., Komppula, M., Laj, P., Li, S.-M., Lunder, C., Marinoni, A., Martins dos Santos, S., Moerman, M., Nowak, A., Ogren, J. A., Petzold, A., Pichon, J. M., Rodriquez, S., Sharma, S., Sheridan, P. J., Teinil, K., Tuch, T., Viana, M., Virkkula, A., Weingartner, E., Wilhelm, R., and Wang, Y. Q.: Characterization and intercomparison of aerosol absorption photometers: result of two intercomparison workshops, Atmos. Meas. Tech. Discuss., 3, 1511–1582, doi:10.5194/amtd-3-1511-2010, 2010. 25998, 25999

Nessler, R., Weingartner, E., and Baltensperger, U.: Adaptation of dry nephelometer measurements to ambient conditions at the Jungfraujoch, 39, 2219–2228, 2005. 26012, 26013

Ogren, J. and Charlson, J.: Implications for models and measurements of chemical inhomogeneities among cloud droplets, Tellus, 44B, 489–504, 1992. 25993

Petzold, A. and Schönlinner, M.: Multi-angle absorption photometry - a new method for the measurement of aerosol light absorption and atmospheric black carbon, 35, 421–441, 2004. 25998, 25999

Pikridas, M., Bougiatioti, A., Hildebrandt, L., Engelhart, G. J., Kostenidou, E., Mohr, C., Prévôt, A. S. H., Kouvarakis, G., Zarmpas, P., Burkhart, J. F., Lee, B.-H., Psichoudaki, M., Mihalopoulos, N., Pilinis, C., Stohl, A., Baltensperger, U., Kulmala, M., and Pandis, S. N.: The Finokalia Aerosol Measurement Experiment – 2008 (FAME-08): an overview, Atmos. Chem. Phys., 10, 6793–6806, doi:10.5194/acp-10-6793-2010, 2010. 25994

Press, W. H., Flannery, B. P., Teukolsky, S. A., and Wetterling, W. T.: Numerical recipes in

ACPD

10, 25991–26044, 2010

Fortran, Cambridge Univ. Press, New York, 2nd edn., 1992. 26004
Randriamiarisoa, H., Chazette, P., Couvert, P., Sanak, J., and Mégie, G.: Relative humidity impact on aerosol parameters in a Paris suburban area, 6, 1389–1407, 2006. 26012
Raut, J.-C. and Chazette, P.: Retrieval of aerosol complex refractive index from a synergy between lidar, sunphotometer and in situ measurements during LISAIR experiment, Atmos. Chem. Phys., 7, 2797–2815, doi:10.5194/acp-7-2797-2007, 2007. 26012
Sciare, J., Bardouki, H., Moulin, C., and Mihalopoulos, N.: Aerosol sources and their contribution to the chemical composition of aerosols in the Eastern Mediterranean Sea during summertime, Atmos. Chem. Phys., 3, 291–302, doi:10.5194/acp-3-291-2003, 2003. 25994
Schkolnik, G., Chand, D., Hoffer, A., Andreae, M.O., Erlick, C., Swietlicki, E., and Rudich, Y.: Constraining the density and complex refractive index of elemental and organic carbon in biomass burning aerosol using optical and chemical measurements, Atmos. Environ., 41, 1107–1118, 2007. 26004
Sheridan, P. J., Jefferson, A., and Ogren, J. A.: Spatial variability of submicrometer aerosol radiative properties over the Indian Ocean during INDOEX, J. Geophys. Res., 107(D19), 8011, doi:10.1029/2000JD000166, 2002. 26012
Sloane, C. S. and Wolff, G. T.: Prediction of ambient light scattering using A physical model responsive to relative humidity: Validation with measurements from Detroit, Atmos. Environ., 19, 669–680, 1985. 26012
Stokes, R. H. and Robinson, R. A.: Interactions in aqueous nonelectrolyte solutions. I. Solute-solvent equilibria, J. Phys. Chem., 70, 2126–2130, 1966. 26003
Swietlicki, E., Zhou, J., Berg, O., Martinsson, B., Frank, G., et al.: A closure study of sub-micrometer aerosol particle hygroscopic behavior, Atmos. Res., 50, 205–240, 1999. 26001
Swietlicki, E., Hansson, H.-C., Hämeri, K., Svenningsson, B., Massling, A., et al.: Hygroscopic properties of submicrometer atmospheric aerosol particles measured with H-TDMA instruments in various environments – a review, Tellus, 60B, 432–469, 2008. 26007, 26016
Tang, I. N. and Munkelwitz, H. R.: Water activities, densities and refractive indices of aqueous sulfates and soldium nitrate droplets of atmospheric importance, J. Geophys. Res., 99, 18801–18808, 1994. 25993, 26001, 26003
Tang, I. N.: Chemical and size effects of hygroscopic aerosols on light scatterring coeffcients, J. Geophys. Res., 101, 19245–19250, 1996. 25993, 26012, 26013
Teinilä, K., Kerminen, V.-M., and Hillamo, R.: A study of size segregated aerosol chemistry in the Antarctic atmosphere, J. Geophys. Res., 105, 3893–3904, 2000. 25999

ACPD
10, 25991–26044, 2010

Twomey, S.: Atmospheric aerosols, 320 pp., Elsevier, New York, 1977. 25993
Vardavas, I. M. and Taylor, F. M.: Radiation and Climate, International Series of Monographs on Physics No. 138, Oxford University Press, 2007. 26014
Van Dingenen, R., Putaud, J.-P., Martins-Dos Santos, S., and Raes, F.: Physical aerosol properties and their relation to air mass origin at Monte Cimone (Italy) during the first MINATROC campaign, Atmos. Chem. Phys., 5, 2203–2226, doi:10.5194/acp-5-2203-2005, 2005. 25994
Wex, H.: Closue and sensitivity studies on physical parameters of rural continental aerosols, Phd. thesis, Leipzig University, 2002. 25996, 26005
Willeke, K. and Baron, P. A.: Aerosol measurement: Principles techniques and applications, Van Nostrand Reinhold, 115 Fifth Avenue, 10003 New York, USA, 1993. 25996
Wiscombe, W. J. and Grams, G. W.: The backscattered fraction in two-stream approximations, J. Atmos. Sci., 33, 2440–2451, 1976. 26015
Zdanovskii, A.: New methods for calculating solubilities of electrolytes in multicomponent systems, Zhur. Fiz. Khim, 22, 1475–1485, 1948. 26003

ACPD
10, 25991–26044, 2010

Table 1. Time period definition. f_{soot} is the mass fraction of soot in particles < 1 µm.

	Date	Origin	f_{soot}	Category
A1	21.09.05 10:30–25.09.05 00:00	Western Mediterranean Sea	2.8 %	marine
A2	27.09.05 18:00–30.09.05 18:00	Black Sea	4.5 %	polluted
A3	01.10.05 22:00–04.10.05 10:00	Western Mediterranean Sea	3 %	marine
A4	05.10.05 00:00–12.10.05 00:00	Black Sea and South-East Europe	5.1 %	polluted

ACPD
10, 25991–26044, 2010

Table 2. Mean hygroscopic growth factors, number fractions, soluble volume fraction of each hygroscopic growth group, total soluble volume fraction and their standard mean deviation for the observed sub-micrometer particle diameters during the campaign.

Hygroscopic growth group	growth factor	number fraction	soluble volume fraction	total soluble volume fraction
D_p = 30 nm				0.52±0.12
More hygroscopic	1.42±0.05	0.79±0.17	0.60±0.09	
Less hygroscopic	1.24±0.05	0.13±0.12	0.31±0.07	
Nearly hydrophobic	1.04±0.06	0.08±0.12	0.04±0.06	
D_p = 50 nm				0.66±0.11
More hygroscopic	1.51±0.06	0.90±0.08	0.70±.011	
Less hygroscopic	1.30±0.05	0.06±0.05	0.36±0.07	
Nearly hydrophobic	1.12±0.07	0.04±0.05	0.12±0.08	
D_p = 80 nm				0.67±0.13
More hygroscopic	1.56±0.06	0.84±0.12	0.74±0.11	
Less hygroscopic	1.36±0.06	0.09±0.07	0.41±0.08	
Nearly hydrophobic	1.17±0.08	0.07±0.08	0.17±0.09	
D_p = 150 nm				0.71±0.14
More hygroscopic	1.59±0.07	0.87±0.07	0.76±0.13	
Less hygroscopic	1.41±0.07	0.07±0.05	0.40±0.09	
Nearly hydrophobic	1.18±0.08	0.06±0.05	0.17±0.08	
D_p = 250 nm				0.74±0.15
More hygroscopic	1.63±0.07	0.85±0.08	0.80±0.14	
Less hygroscopic	1.40±0.09	0.07±0.06	0.44±0.14	
Nearly hydrophobic	1.19±0.08	0.07±0.05	0.18±0.09	
D_p = 350 nm				0.70±0.16
More hygroscopic	1.63±0.08	0.77±0.12	0.81±0.15	
Less hygroscopic	1.42±0.11	0.10±0.08	0.45±0.16	
Nearly hydrophobic	1.18±0.08	0.14±0.10	0.16±0.08	

ACPD
10, 25991–26044, 2010

Table 3. Mean hygroscopic growth factors, number fractions and standard mean deviation for particles with a dry mobility diameters D_p of 1.0 and 1.2 µm.

Hygroscopic growth group	aerodynamic growth factor	number fraction
D_p = 1000 nm		
More hygroscopic	1.20±0.04	0.60±0.12
Less hygroscopic	1.04±0.05	0.12±0.07
Nearly hydrophobic	1.03±0.05	0.28±0.10
D_p = 1200 nm		
More hygroscopic	1.31±0.14	0.38±0.22
Less hygroscopic	1.12±0.05	0.31±0.18
Nearly hydrophobic	1.09±0.08	0.31±0.18

ACPD
10, 25991–26044, 2010

Table 4. Correlation between calculated and measured optical properties (σ_j^c and σ_j^e). Here, $\sigma_j^c = b \cdot \sigma_j^e$, with adjusted correlation coefficient (R^2).

	Slope (b)	R^2
$\sigma_{sp,450\,nm}$	0.999	0.992
$\sigma_{sp,550\,nm}$	1.069	0.995
$\sigma_{sp,700\,nm}$	1.197	0.992
$\sigma_{bsp,450\,nm}$	0.949	0.979
$\sigma_{bsp,550\,nm}$	0.915	0.986
$\sigma_{bsp,700\,nm}$	0.888	0.948
$\sigma_{ap,630\,nm}$	0.991	0.999

ACPD
10, 25991–26044, 2010

Table 5. Mean values of measured total scatter and absorption coefficients (Mm^{-1}) and retrieved refractive index, divided into marine air masses and continentally polluted air masses.

	Marine	Continental Polluted
$\bar{\sigma}_{sp,450\,nm}$	16±6	63±15
$\bar{\sigma}_{sp,550\,nm}$	10±4	44±11
$\bar{\sigma}_{sp,700\,nm}$	6±2	26±6
$\bar{\sigma}_{bsp,450\,nm}$	1.8±0.6	6.9±1.5
$\bar{\sigma}_{bsp,550\,nm}$	1.5±0.5	5.7±1.2
$\bar{\sigma}_{bsp,700\,nm}$	1.2±0.5	4.5±1.0
$\bar{\sigma}_{ap,630\,nm}$	0.8±0.3	5.2±1.3
$\bar{n}_r$	1.48±0.04	0.01±0.003
$\bar{n}_i$	1.50±0.02	0.02±0.002

ACPD
10, 25991–26044, 2010

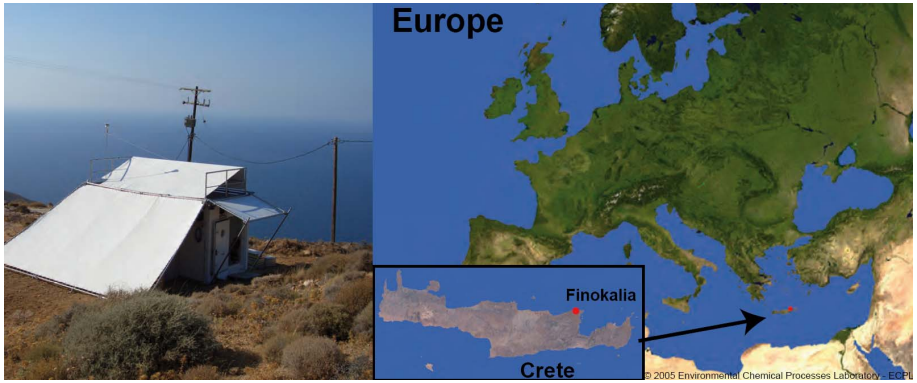

Fig. 1. Atmospheric aerosol measurements during ARIADNE: container laboratory (left), and location of the Finokalia research site on Crete, in the eastern Mediterranean (right).

ACPD
10, 25991–26044, 2010

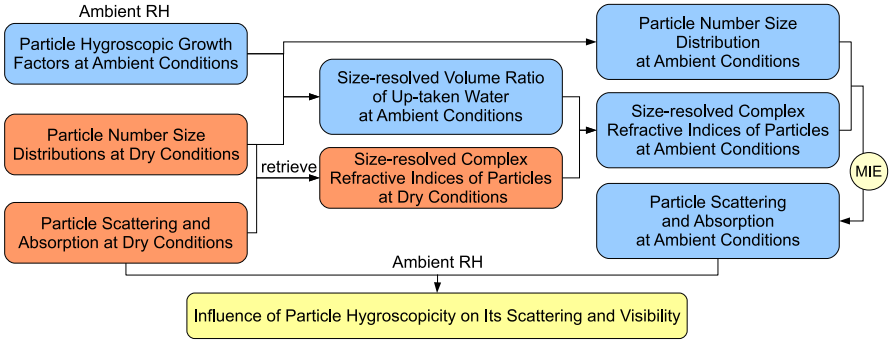

Fig. 2. Simulating aerosol properties at ambient conditions using the optical model.

ACPD
10, 25991–26044, 2010

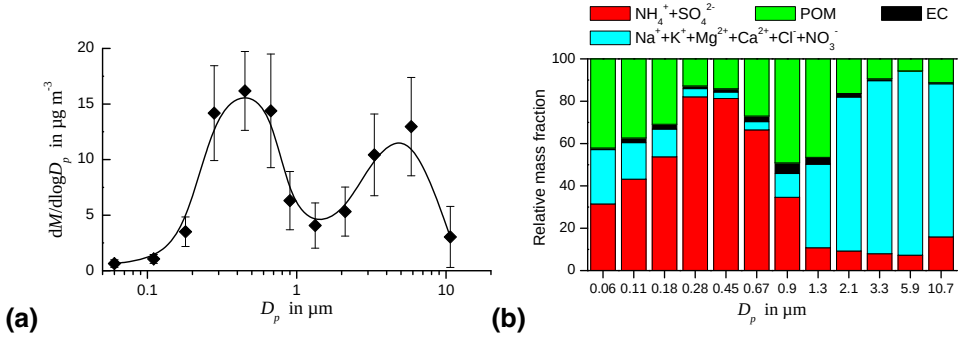

Fig. 3. Average characteristics of ambient particles during ARIADNE. **(a)** total mass distribution with one standard deviation. **(b)** chemical composition, classified into four groups including ammonium sulfate ($NH_4^+ + SO_4^{2-}$), fresh and processed sea-salt ($Na^+ + K^+ + Mg^{2+} + Ca^{2+} + Cl^- + NO_3^-$), elemental carbon (EC) and particulate organic matter (POM).

ACPD
10, 25991–26044, 2010

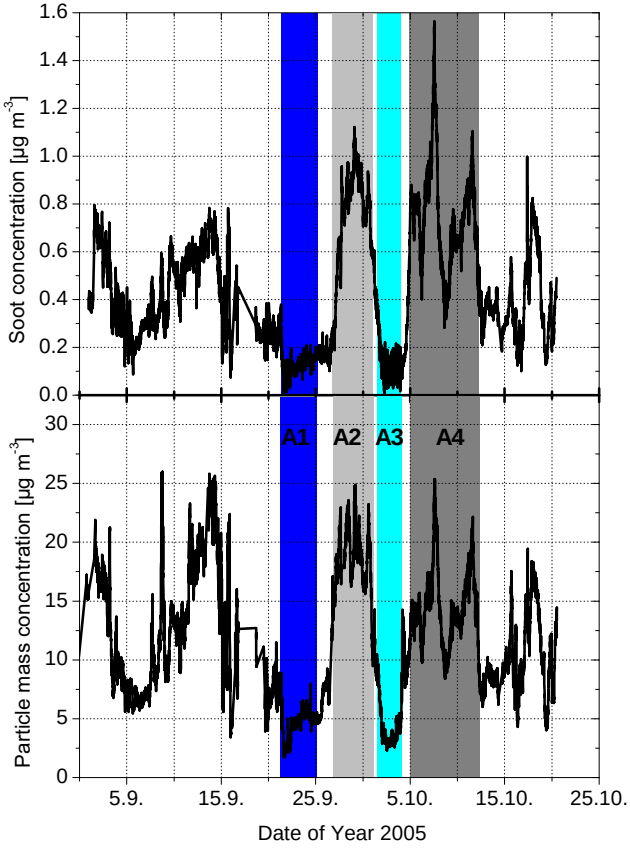

Fig. 4. Time series of the soot mass concentration (MAAP), and the total particle mass concentration derived from DMPS/APS measurements. A1–A4 indicate four time periods representing rather distinct air mass types.

ACPD
10, 25991–26044, 2010

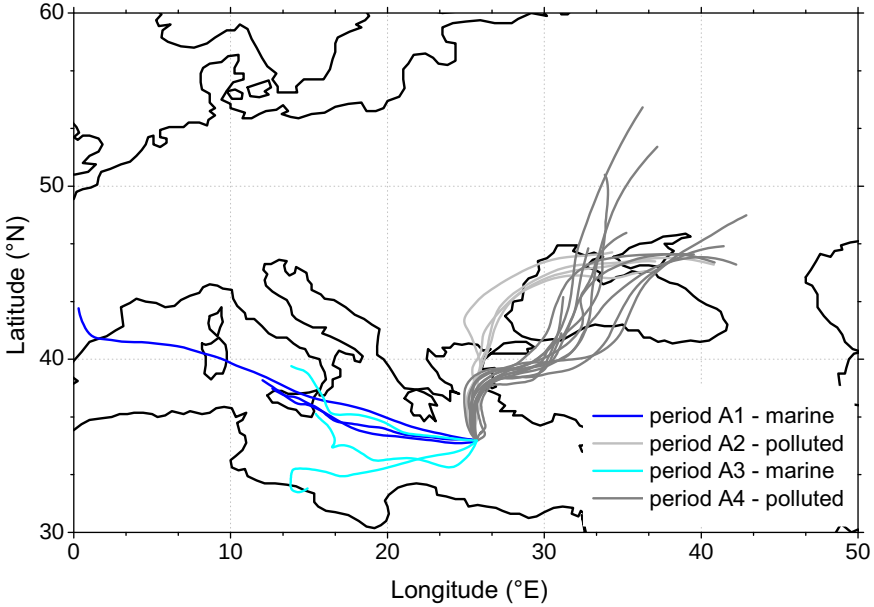

Fig. 5. Backward trajectories (duration 72 h, start height 500 m) during ARIADNE, as calculated using the NOAA HYSPLIT model.

ACPD
10, 25991–26044, 2010

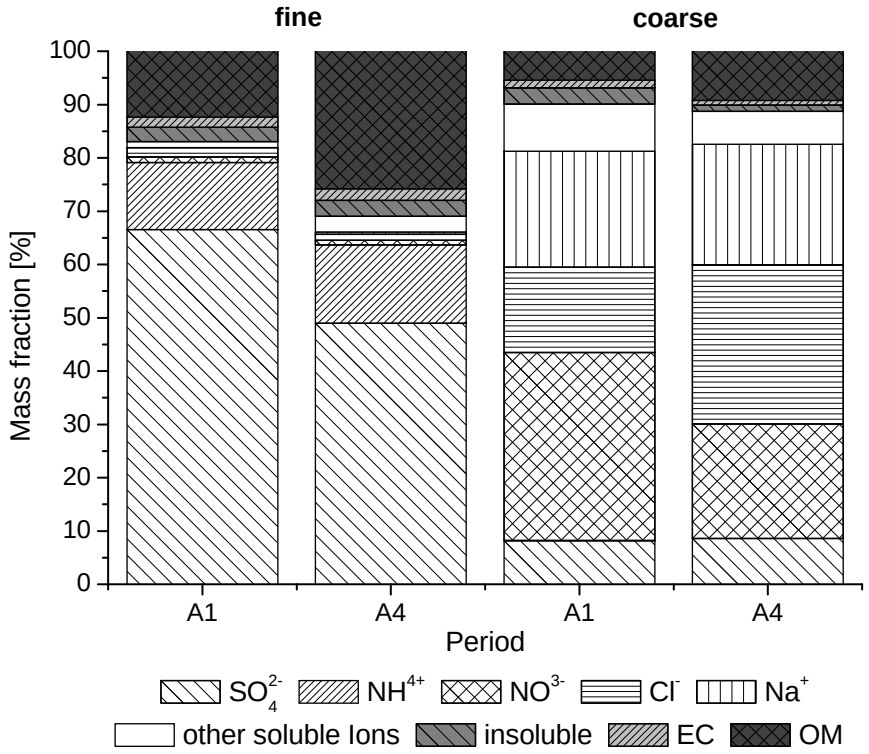

Fig. 6. Chemical composition of fine and coarse particles during the time periods A1 (marine) and A4 (continentally-polluted).

ACPD
10, 25991–26044, 2010

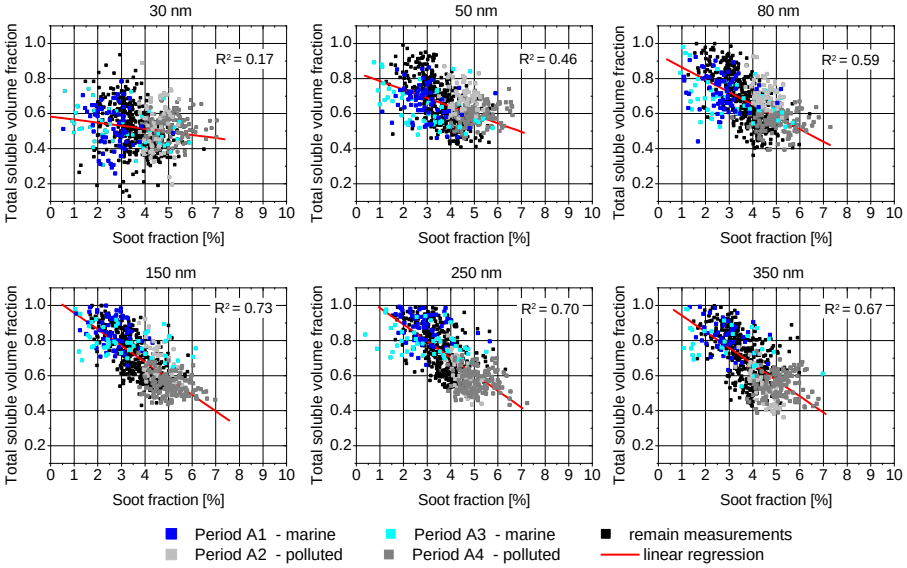

Fig. 7. Correlation between the total soluble volume fraction and the soot fraction over the entire measurement period for fine and coarse particles.

ACPD
10, 25991–26044, 2010

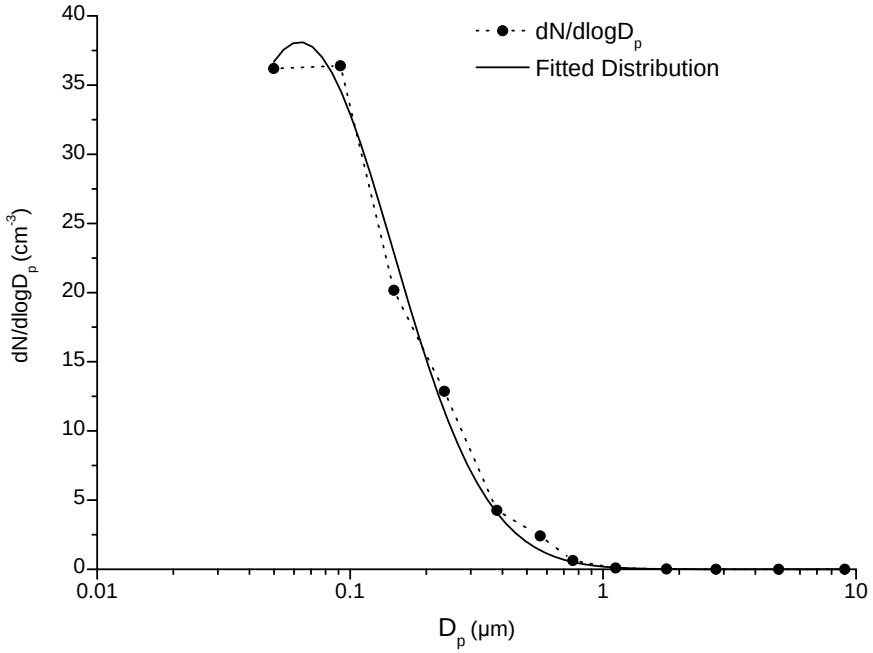

Fig. 8. Mean number size distribution for elemental carbon derived from the size segregated chemical analysis.

ACPD
10, 25991–26044, 2010

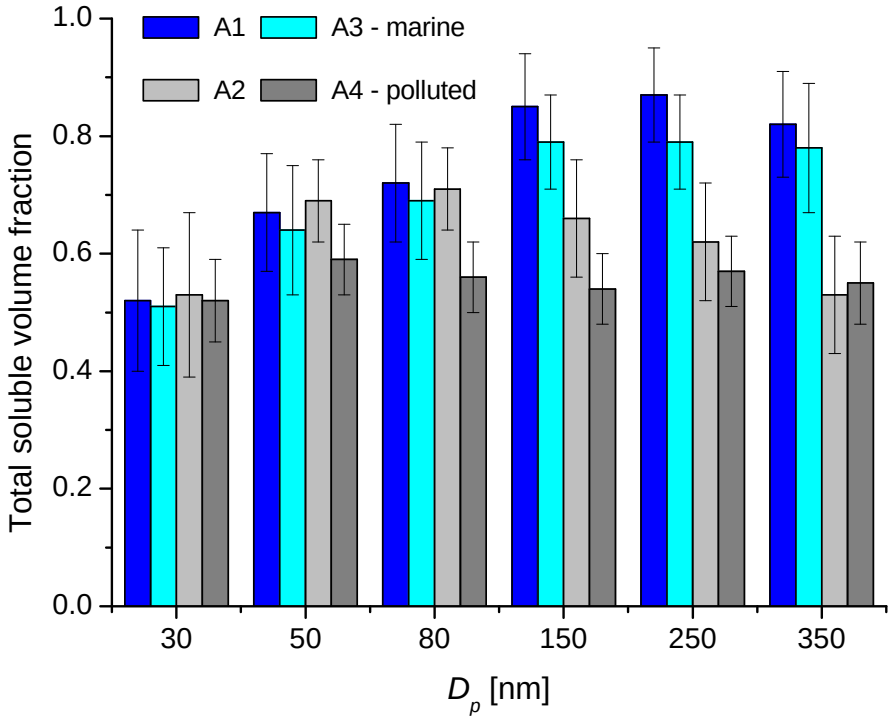

Fig. 9. Mean total soluble volume fraction as a function of particle size during different air mass periods. The plotted error bars are showing the corresponding standard mean deviation.

ACPD
10, 25991–26044, 2010

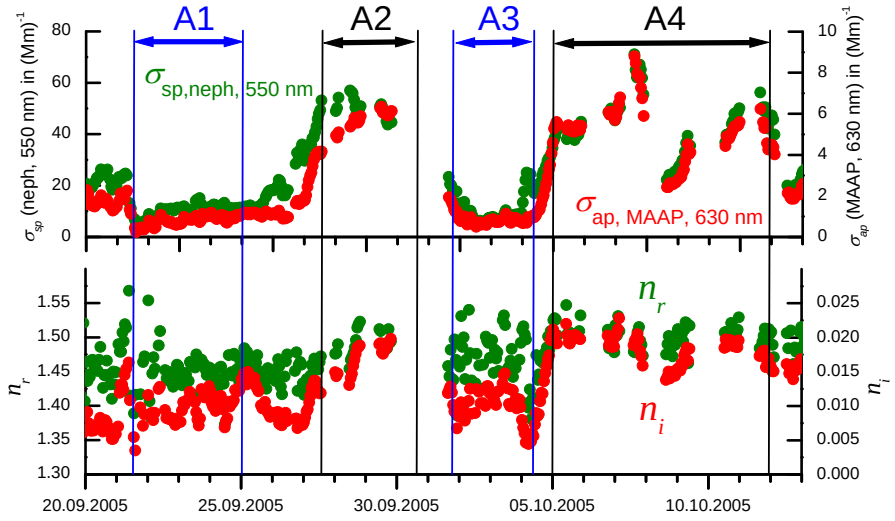

Fig. 10. Time series of **(a)** total scattering coefficients at 550 nm ($\sigma_{sp,neph,550\,nm}$) and absorption coefficients at 630 nm ($\sigma_{ap,MAAP,630\,nm}$) measured by the nephelometer and the MAAP, as well as **(b)** real and imaginary parts of the retrieved refractive indices (n_r and n_i). Periods dominated by marine air masses (A1 and A3) and continentally-polluted air masses (A2 and A4) are indicated.

ACPD
10, 25991–26044, 2010

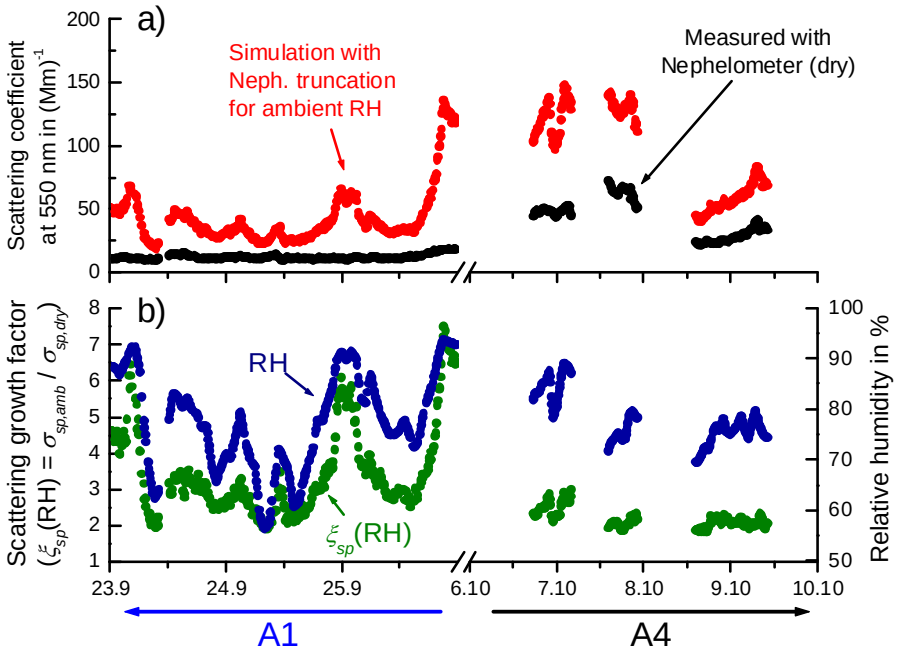

Fig. 11. Time series of modeled aerosol scattering coefficients (550 nm) at ambient conditions and the aerosol scattering coefficients (550 nm) measured by a nephelometer at dry conditions (top Figure), as well as ambient relative humidity and scattering growth factor ($\xi_{sp}(RH) = \sigma_{sp,amb}/\sigma_{sp,dry}$) (bottom Figure) for both marine (m, 23–25 September 2005) and continentally-polluted (cp, 6–9 October 2005) cases.

ACPD
10, 25991–26044, 2010

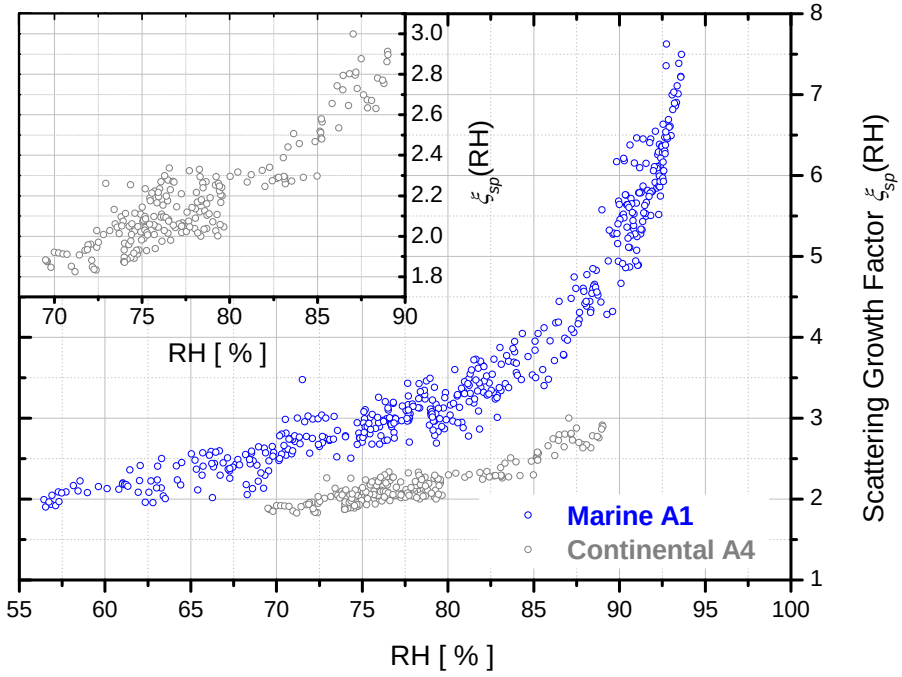

Fig. 12. Growth factors of particle scattering ($\xi_{sp}(RH) = \sigma_{sp,amb}/\sigma_{sp,dry}$) as a function of relative humidity (RH). The data sets were classified into two cases, marine (23–25 September 2005) and continentally-polluted (6–9 October 2005), with a subset containing the zoom-in pattern of the continentally-polluted case.

ACPD
10, 25991–26044, 2010

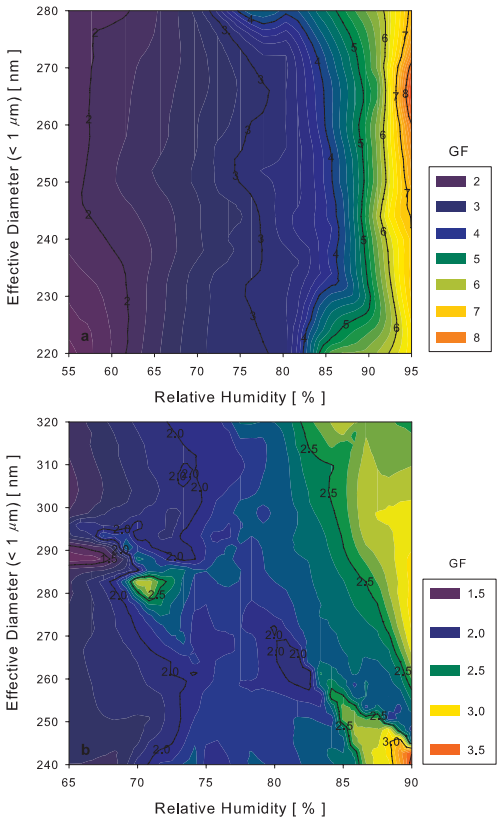

Fig. 13. Contour plots of scattering growth factors ($\xi_{sp}(RH) = \sigma_{sp,amb}/\sigma_{sp,dry}$) as a function of relative humidity and effective diameter ($D_{p,eff}$) of the submicrometer particle number size distributions at dry conditions for **(a)** marine (23–25 September 2005) and **(b)** continentally-polluted (6–9 October 2005) cases. The data sets were smoothed by LOESS method.

ACPD
10, 25991–26044, 2010

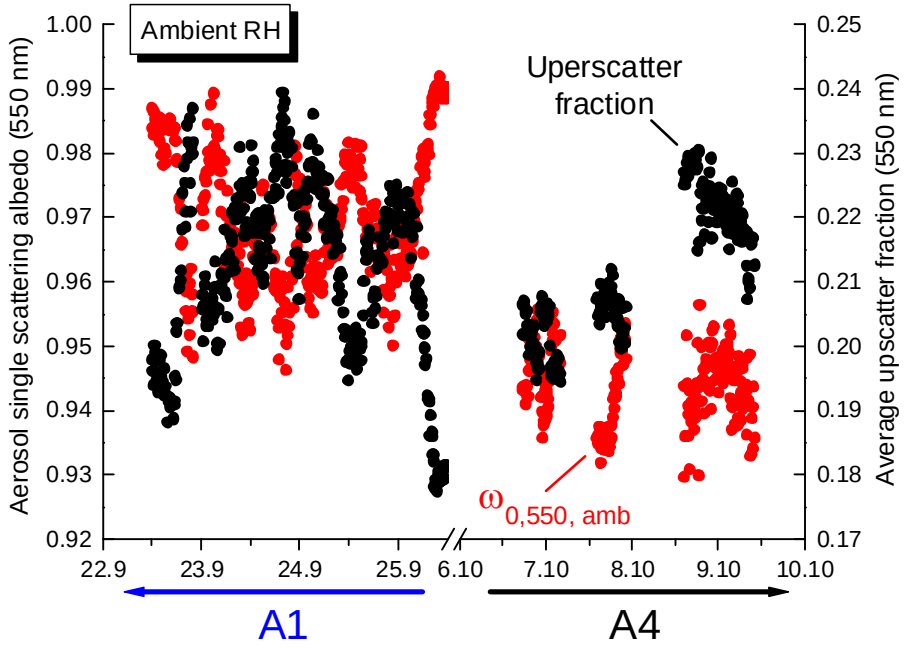

Fig. 14. Time series of the calculated aerosol single scattering albedo ($\omega_{0,550\mathrm{nm,amb}}$) and estimated upscatter fraction ($\overline{\beta}_{550\mathrm{nm,amb}}$) at ambient conditions for both marine (A1) and continentally polluted (A4) cases.

ACPD
10, 25991–26044, 2010

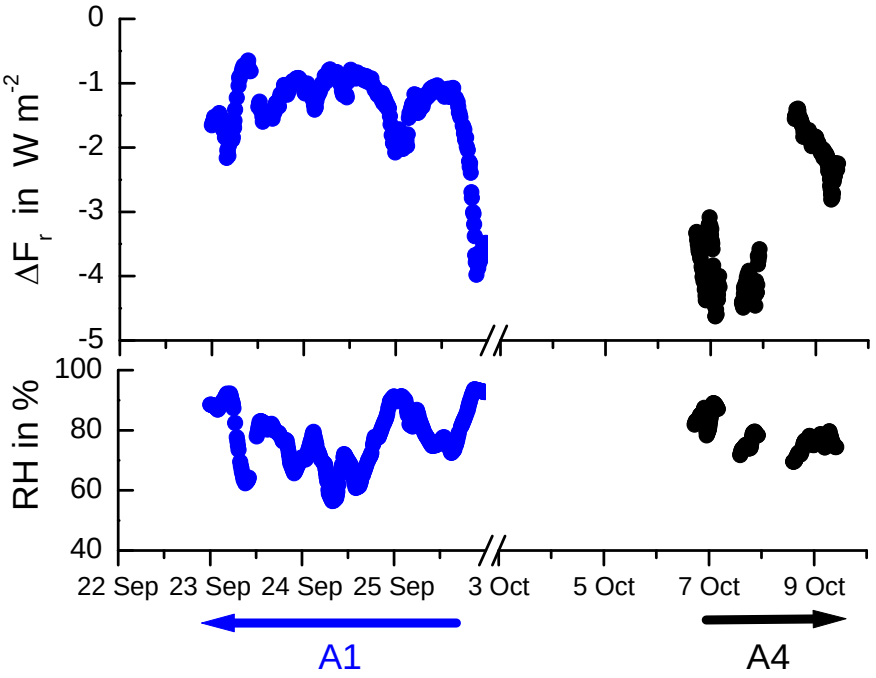

Fig. 15. Time series of the calculated aerosol direct radiative forcing (ΔF_r) at ambient conditions as well as the ambient relative humidities (RH) for both marine (A1) and continentally polluted (A4) cases.

ACPD
10, 25991–26044, 2010